



Laser beam remelting of stainless steel plate for cladding and comparison with conventional CMT process

Ivan Bunaziv¹ · Xiaobo Ren² · Anette Brocks Hagen¹ · Even Wilberg Hovig² · Ivana Jevremovic¹ · Sverre Gulbrandsen-Dahl³

Received: 7 February 2023 / Accepted: 7 May 2023 / Published online: 22 May 2023
© The Author(s) 2023

Abstract

Progressing towards circular economy requires smarter and more efficient use of energy and resources. Laser beam can be efficient and flexible tool for melting different metals, commonly used in cladding and additive manufacturing (AM) with a wire and powder feedstock. As an alternative, feedstock in the form of plates and sheets can be used for cladding to achieve corrosion resistant surfaces. Compared to powder or wire, plates are easier to process, less costly to use, and may come as scrap metal. This leads to smarter and more efficient resource utilization. However, processing plates in such way is not mature and requires more in-depth investigation to be competitive with well-established methods. In this work, 2.0 mm thick 316L stainless steel plates were remelted by a high-power fibre laser beam for cladding on carbon steel substrates. It was compared to the conventional cold metal transfer (CMT) welding-based arc cladding which is frequently used due to a low heat input. In the first phase, different defocusing distances were studied to understand the laser remelting process capabilities to optimize the productivity. It was found that a highly defocused laser beam provided unstable melt pool conditions with low track quality. Compared to CMT, the laser remelting provided enhanced productivity, reduced heat input by 50% per pass, and lower distortions. Microhardness testing showed an increase in hardness in the intermediate layer towards the fusion line due to carbon diffusion. Despite a higher delta ferrite formation in laser-remelted tracks, a comparable corrosion protection to CMT was observed. The proposed method is promising for reducing CO₂ emissions with respect to reusing scrap metal in the form of plates or use of ordinary plates instead of filler wires which opens possibilities for further enhancements.

Keywords Laser beam · Cladding · Recycling · Stainless steel · Microstructure · Corrosion resistance

1 Introduction

Recently, European industry has been influenced by the Resource Efficiency Roadmap (European Commission, COM/2011/0571) and the Renewable Energy Directive with the European Green Deal (European Commission, COM/2019/640), which aim to reach CO₂ neutrality by 2050 across the continent. The utilization of scrap metal directly for production, the direct reuse, can contribute to

the transition strategy. Moreover, the process is excellent in conjunction with the circular economy strategy development and the Circular Economy Action Plan (European Commission, COM/2020/98) introduced in 2020. The laser beam is a flexible tool for melting various metals; thus, various shape of filler materials can potentially be utilized. One of them can be simple waste sheets in the form of an ordinary plate, see Fig. 1. Remelting of plates for cladding purposes has been used extensively used by arc welding in heavy industry but not by laser beam and has not been widely considered before. Important to note that in this work, plates for experiments were ordinary stainless steel plate cuts with a rectangular shape but it can be any waste sheet from production even though it may have a more complex shape. Moreover, plates for remelting may potentially consist of highly compressed mill chips. However, such products were not available and was not explicitly published so far according to author's knowledge. Therefore, in this manuscript,

✉ Ivan Bunaziv
ivan.bunaziv@sintef.no

¹ Materials and Nanotechnology, SINTEF Industry, Torgarden, P.O. Box 4760, NO-7465 Trondheim, Norway

² Metal Production and Processing, SINTEF Industry, NO-0314 Oslo, Norway

³ Materials Technology, SINTEF Manufacturing, P.O. Box 163, NO-2831 Raufoss, Norway

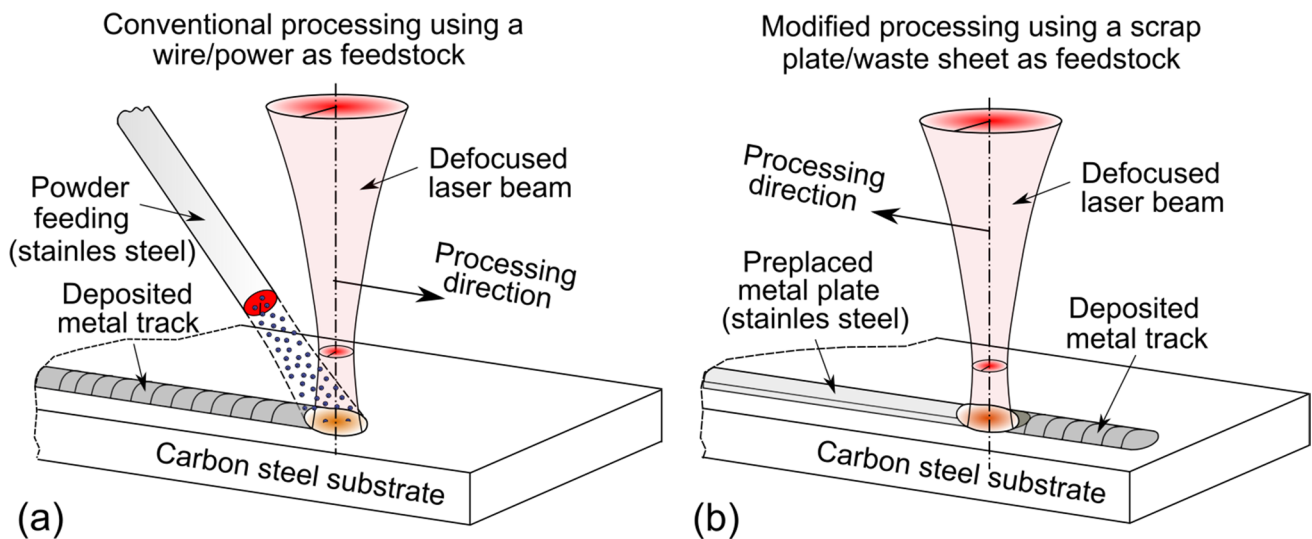


Fig. 1 Comparison of **a** conventional cladding/additive manufacturing with **b** fundamental idea of utilization of preplaced scrap/plate metal by high-power laser beam remelting

we use the term of the feedstock as laser-remelted plates, or scrap metal. Reuse of waste sheets may offer a tremendous economic advantage since they are subjected to remelting in the factory furnaces to create new products such as rolled plates, wire or some kind of strips. By using waste sheets directly as the feedstock there is no need to remelt it, which will conserve much energy and resources. Scrap metal can be directly utilized to refurbish/repair existing products or create a new product. It may not be viable to use the high-power laser beam for recycling aluminium since it melts at low temperatures and possesses high reflectivity. In this case, the arc process may be more suitable. However, such processing is more viable for steels due to their high melting point and low reflectivity, which is more appropriate for 1 μm wavelength high-power Yb: fiber/disk laser systems. Scrap/plate metal remelting is more related to surface cladding and is an important process for surface modification to increase corrosion and/or wear resistance. The use of laser beam for cladding is more flexible than arc since it can use filler wire, powder, and even combination of both in more simple way. Surface cladding can be considered a branch of additive manufacturing and termed as directed energy deposition (DED) [1].

For many decades, surface cladding has been mainly performed via conventional arc welding processes. Submerged arc welding (SAW) provides high production rates (5–10 kg/h) with a single-wire at high energy efficiency (> 90% of energy is used for melting) [2]. However, it is more suitable for flat surfaces due to the used granular flux and high heat input restrict its applicability to thinner and smaller parts. Gas metal arc welding (GMAW) is another widely used process used for cladding due to lower

heat inputs compared to SAW but with lower productivity (6–8 kg/h) with a single-wire [3]. Multi-wire SAW may provide up to 40 kg/h deposition but at excessive heat input and dilution, which limit its use to larger parts. Dilution in cladding describes an amount of melted base metal or substrate (which is usually non-corrosion) mixed with more expensive clad metal with high corrosion resistance meaning that dilution must be minimized to achieve higher quality product. Another high-deposition method (> 20 kg/h) is electroslag strip arc cladding, but it also introduces high heat input. Recently, an emerging cold metal transfer (CMT) arc process has been frequently used for cladding and is more applicable for additive manufacturing (AM). CMT provides lower heat inputs than GMAW with more control for metal deposition, thus may be applicable for the deposition of thin clads/surfaces (< 3 mm).

For many years, laser powder deposition has been widely used with a fine spherical powder (50–200 μm in diameter) as feedstock, which is usually produced by gas atomization process. Metallic powder feedstock is expensive and requires a strong justification for its use. Moreover, due to high complexity in laser beam melting of powder particles and their deposition physics on a surface, porosity and cracking are common issues according to the comprehensive review done by Zhu et al. [4]. The productivity of a typical laser powder cladding using a multi-kilowatt laser power is rather low (in terms of kg per hour) compared to multi-wire SAW; only 2–4 kg/h [5]. However, high-power lasers can have a large rectangular spot geometry and may exceed 20 mm in width and this can reach respectable covering areas and deposition rates up to 15 kg/h [6], especially when thin metallic coating is

required. A rough surface quality may be produced without optimized parameters and powder utilization efficiency is only up to 80% [7]. However, dilution can be as low as 3–5% and even 1% with optimized parameters, which may provide a great corrosion resistance and mechanical properties due to high metallurgical bonding. Moreover, it is not restricted to flat surfaces. Laser wire deposition may provide improved deposition rates close to GMAW but with higher dilution. A typical application of cladding using conventional feedstock is illustrated in Fig. 1. There has been a proliferation of research articles concentrated on improving metallurgy through advanced alloying; henceforth, productivity and efficiency of the process itself have been overlooked.

Zhang et al. [8] attempted to use a scrap metal as compressed iron chips as base metal in hot rolling with stainless steel to produce a clad plate. However, the studied thicknesses were limited (< 3 mm), and the use of scrap metal seems to be much more viable for anti-corrosive surface. The use of recycled material as a mechanically produced small powder from mill chips by multi-stage ball milling, was adopted and published by some researchers [9–11]. However, the proposed method did not receive much attention yet. Researchers from Luleå University of Technology [12] made the first attempts in 2017 for cladding/additive manufacturing using a remote fusion cutting (RFC) with limited success where a clad plate was lifted above a substrate. Such process is complex with many parameters to be optimized, thus did not receive much attention. However, its adaptation for cladding purposes is more viable since no high accuracy of tracks is needed compared to AM. The idea was to melt the lifted sheet metal by a laser beam so that the melt droplets from a cutting kerf surface deposited on a substrate underneath. Fairly good tracks in appearance can be made by such process, especially for conventional carbon steel. It requires no special cutting nozzle, and standard laser beam equipment can be utilized. This process is more cost-efficient than the multi-stage re-milling of mill chips offering higher deposition rates. However, the researchers did not use stainless steel for cladding purposes. In the subsequent work [13], the stainless steel was deposited on a carbon steel substrate with limited success. Therefore, the proposed process with lifted plate above substrate is complex and requires a significant optimization of parameters and understanding of the process physics. Tuominen et al. [14] demonstrated use of high-power laser remelting of Inconel 625 strips for cladding on carbon steel shafts reaching 8 kg/h productivity to deposit 2 mm thick clad layer. However, the process requires special equipment due to the angled feeding of the strips, and mechanical properties have not been revealed with the vaguely described corrosion properties of the produced clads. So far, no further development has been published in this direction.

Laser remelting of a pre-placed plate on a substrate may offer a smooth track appearance with optimized parameters, relatively easy setup similar to laser welding, good process stability, and high degree of material utilization compared to power-based processes. This process may be similar to the laser sheet lamination additive processing but with the use of high-power laser outputs. Moreover, it may offer a unique opportunity for the simple and easy preplacement of the interlayers due to the flat surfaces between the plate and substrate to enhance properties. As an example, a thin pure nickel layer may prevent hydrogen diffusion and increase fracture toughness [15], and a pure iron layer may significantly increase the strength by the prevention of carbon diffusion [16]. In arc-based processes, this can be achieved only via modification of a filler wire which is more complicated and limited due to the production of such filler materials. The plate laser remelting process seems simple, but it may be challenging to achieve tracks with a good quality. The melt may be unstable causing spattering and a poor-quality surface. Optimization of parameters and stability are the keys to success in the further development of this process. Heat inputs should be restricted to eliminate distortions, and low dilution should be achieved. The process is mostly suitable for flat surfaces but can be modified when needed.

Austenitic stainless steels (ASST) are common in anti-corrosive application due to their good mechanical and corrosion properties and relatively low price compared to Ni-based alloys. For example, 304 ASST is a foundation alloy, while 316L alloy grade containing 2–3% Mo and reduced carbon content provides improved resistance to intergranular attack and stress corrosion cracking. Therefore, 316L has a high potential for cladding of carbon steels. The objective of this work is to demonstrate laser beam remelting to smartly utilize preplaced 316L scrap/plate metal (in the form of plates, 2.0 mm in thickness) for surface cladding purposes, which may be further developed as an AM process to build larger parts but requires additional planning in optimization of materials with certain dimensions. This work demonstrates the effectiveness of laser process compared to laser beam remelting in term of productivity and quality. Moreover, the work clearly shows significant advantages to use an ordinary plate for flat surfaces instead of filler wires. Optimization testing was conducted for laser beam remelting to understand the process limitations to maximize productivity by large volume remelting with higher laser powers. Refined parameters with a stable processing were adopted to remelt representative amounts of the plate and compared to the conventional CMT arc process. Extensive studies were performed on the prediction of microstructure using different prediction models and experimental/numerical methods. The laser remelting process provided finer dendritic structure with improved mechanical properties and a slightly increased corrosion resistance compared to CMT.

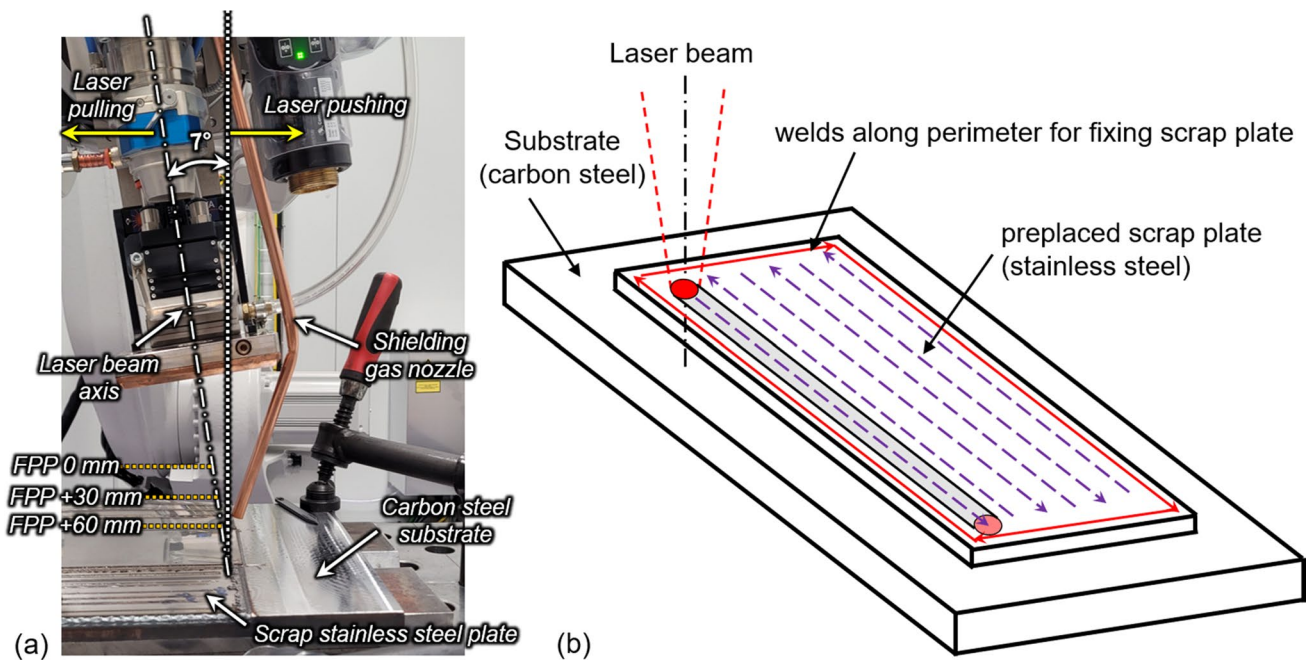


Fig. 2 **a** Experimental setup for laser remelting and **b** schematic illustration of preplaced scrap/metal plate on substrate utilization. *FPP* is focal point position

The corrosion resistance was still lower than 316L initial plate. A further development may improve capabilities and quality of the laser remelting clads.

2 Methodology

2.1 Equipment and materials

A continuous wave randomly polarized multi-mode 16 kW ytterbium fiber laser (IPG Photonics YLS-16000-S2 type model) was used in the experiments with the following parameters: fiber core diameter 300 μm , beam parameter product 12 mm•mrad, and 1070 nm wavelength. The laser beam had Gaussian heat distribution and had the following optical parameters: 300 mm focal length, the smallest focused spot size on the surface is 512 μm in diameter (as measured), and Rayleigh length of 5.6 mm (as measured). The laser beam was longitudinally inclined by 7° from the normal towards the welding surface to eliminate back reflections. Pure argon (99.995%) was used as shielding gas supplied by shielding gas nozzle to the

process area. Welds were deposited with an articulated robot. The general setup used is shown in Fig. 2. In this work, we used a common zig-zag hatching pattern of the laser beam direction path, also referred to as bi-directional or raster hatching pattern.

A conventional structural low carbon steel (S420ML grade) was used as a base substrate and was cut into $300 \times 300 \text{ mm}^2$ with a thickness of 15 mm. Machining was used on the top of surface to remove all mill scale (iron surface oxides). Austenitic stainless steel 316L plate (2.0 mm in thickness) as feedstock was pre-placed on the top of the carbon steel substrate. The feedstock plate was tack welded across perimeter to ensure rigidity. Then, the plate was melted by laser beam tracks similarly to welding. The chemical composition of the substrate and feedstock provided in Table 1.

2.2 Process variables

The melting parameters for the preplaced stainless steel on the surface of substrate are listed in Table 2. Here, different combinations of laser powers and travel speeds were used to find optimized parameters. Different defocusing distances,

Table 1 Chemical composition (wt.%) of base metal substrate, preplaced scrap/metal plate, and stainless steel filler wire. The base metal contains small amounts of Al, Nb, and Ti (<0.03 wt.%)

Element	C	Si	Mn	P	S	V	Ni	Cr	Cu	Mo	Nb	Fe
Substrate	0.10	0.08	1.97	0.007	0.001	0.01	0.70	0.07	0.18	0.1	-	Bal
316L plate/wire	0.025	0.80	1.70	<0.02	<0.015	-	11.7	18.4	0.13	2.6	0.02	Bal

Table 2 Process variables used for experiments. Experiments no. 14–17 had the zig-zag hatching pattern for full scale remelting of preplaced stainless steel plates on carbon steel substrate

Remelt no. (set no.)	Laser power (kW)	Travel speed v_s (m/min)	FPP (mm)	Heat input (kJ/mm)	Beam diameter at the plate surface (mm)	Power density at the surface (kW/mm ²)	Beam offset (mm)
1 (i)	4.0	2.0	+30	0.08	2.2	1.82	-
2 (i)	5.0	2.0	+30	0.11	2.2	2.27	-
3 (i)	6.0	2.0	+30	0.13	2.2	2.73	-
4 (ii)	4.0	1.5	+30	0.11	2.2	1.82	-
5 (ii)	5.0	1.5	+30	0.14	2.2	2.27	-
6 (ii)	6.0	1.5	+30	0.17	2.2	2.73	-
7 (iii)	6.0	1.5	+60	0.17	4.0	1.50	-
8 (iii)	7.0	1.5	+60	0.20	4.0	1.75	-
9 (iii)	8.0	1.5	+60	0.22	4.0	2.00	-
10 (iii)	9.0	1.5	+60	0.25	4.0	2.25	-
11 (iii)	10	1.5	+60	0.28	4.0	2.50	-
12 (iv)	7.0	1.0	+60	0.55	4.0	1.75	-
13 (iv)	5.0	1.0	+60	0.21	4.0	1.25	-
14 (v)	5.0	2.0	+30	0.11	2.2	2.27	2.5
15 (v)	6.0	2.0	+30	0.13	2.2	2.73	2.5
16 (v)	6.0	2.0	+30	0.13	2.2	2.73	2.2
17 (v)	5.5	2.0	+30	0.12	2.2	2.50	1.8

based on the focal point position (FPP), were tested for a larger melting area to achieve maximum productivity. Experiments were divided into sets (i, ii, iii etc.) which means that a certain number of experiments were made with the variation of one-variable-at-time (OVAT) strategy to understand the effect of variables on the track quality and processing efficiency.

The total line energy input Q (kJ/mm) per track is calculated according to the following formula: $Q = (60 \cdot P_L \cdot \eta_L) / (1000 \cdot v_t)$, where P_L is laser power (in kW), v_t is travel speed (m/min), and η_L is laser beam efficiency factor (absorption coefficient was taken as 0.7).

2.3 Calculations of dilution

The change in chemical composition of the remelted substrate (or base metal) made from a carbon steel is expressed through dilution (measured in %) with the preplaced stainless steel plate (for laser remelting case) or added filler wire (for CMT cladding case) which was calculated based on the following equation [17]:

$$\text{Dilution} = \frac{\text{Area of melted carbon steel plate}}{\text{Total area of fused zone}} \quad (1)$$

2.4 Microstructural analysis

The samples were prepared using standard (EN ISO 17639:2003) metallographic preparations with grinding and

diamond polishing for EDS analysis and etched for microscopy investigation. The polished samples were etched with Marbles reagent consisting of 50 mL H₂O, 10 g CuSO₄, and 50 mL HCl. Both carbon and stainless steel areas were acceptable for microstructural analysis. The microstructure was studied by optical microscope (OM) and field emission scanning electron microscope (SEM) using FEG-SEM, Zeiss Ultra 55 operating at 15–20 kV acceleration voltage. Two different modes were used: the back-scatter electron detector (QBSD) and the secondary beam (SE2). Energy-dispersive X-ray spectroscopy (EDS) was performed using a JEOL JXA-8500F operating at 15 kV and 30 nA. Line scans with a 1- μ m step size were conducted across the clad, intermediate layer, and the HAZ. In addition, point analysis from the top to the centre of the clad was conducted.

2.5 Microhardness and nano-hardness measurements

The Vickers microhardness test was performed based on ISO 22826:2005 in accordance with ISO 6507–1:2018. The region of interest is the intermediate layer and surrounding areas. Microhardness load is chosen based on the grain size and microstructural features. The intermediate layer between the clad layer and the carbon steel base plate is narrow. Therefore, two different loads (25 gf and 200 gf) were selected and compared, HV_{0.025} and HV_{0.2}, respectively. A higher load (HV_{0.2}) may provide inadequate hardness values by capturing larger areas with a significantly lower/

higher hardness. Therefore, additional hardness tests were performed with significantly lower load to provide more adequate understanding of the intermediate layer's hardness.

In addition to the microhardness testing, the nanoindentation test was carried out to determine hardness across the intermediate layer which provides more insightful data about the plasticity and interaction with the adjacent microstructures. The experiments were performed using a Hysitron TI950 triboindenter with a scanning probe microscopic (SPM) imaging option. An array of 3×30 indents (an area of about $200 \mu\text{m}$ was indented across the area of interest) was located across the intermediate layer and CGHAZ with a peak load of $3000 \mu\text{N}$ using the standard three-sided Berkovich tip (half angle of 65.35°). The spacing of $10 \mu\text{m}$ between indents was used to avoid the influence of the work hardening from the adjacent indent's plasticity zone. A predefined grid with the area dimension of $16 \times 12 \mu\text{m}$ and an indent spacing of $0.5 \mu\text{m}$ were used to perform a total of 300 indents for the CMT-cladded specimen. Tests were performed in a load-controlled mode with a peak load of $500 \mu\text{N}$. During testing, the applied load and indenter displacement is continuously measured. The load–displacement data for each indent is continuously constructed from the applied load and the displacement of the tip, from which the reduced modulus and hardness were calculated by the Oliver and Pharr method [18].

2.6 Corrosion testing

Different electrochemical techniques were employed to investigate the corrosion stability of samples obtained by the laser-remelted cladding compared to those obtained by the CMT arc cladding. The electrochemical measurements were conducted in a 3.5 wt.% NaCl using a conventional three electrode cell assembly on steel as a working electrode (tested area was 3.14 cm^2); Pt mesh was used as the counter electrode and a saturated silver/silver chloride (Ag/AgCl) as a reference electrode. Samples compared in this study are bare 316L steel samples as baseline, samples obtained by CMT arc cladding and those obtained by laser remelting process. Electrochemical measurements were carried out subsequently after 1 h of open circuit potential, E_{ocp} , measurements. E_{ocp} was monitored to get a stable potential with time before carrying out the corrosion tests. Linear polarization resistance (LPR) measurements were performed from a cathodic potential of -20 mV to an anodic potential of 20 mV with respect to the E_{ocp} at a scan rate 0.125 mV/s . The corrosion rate was evaluated by means of potentiodynamic sweep (PDS) from a cathodic potential of -0.60 V to an anodic potential of 0.60 V with respect to the E_{ocp} , at a scan rate of 0.168 mV/s . All the electrochemical measurements were carried out using a reference 600 TM Potentiostat/Galvanostat/ZRA (Gamry Instruments, Inc. Warminster, PA, USA).

2.7 Numerical simulation

The numerical process simulation was carried out with the finite element (FE) commercial tool *Simufact Welding 2021*. The laser heat source is estimated as a conical heat source with an upper radius of 0.3 mm , lower radius of 0.15 mm , and a depth of 2.0 mm . The efficiency was calibrated to 0.6 by comparing the simulated melt pool geometry to the experimental micrographs. External natural convection was assumed, and in the interface between stainless steel and carbon steel a constant contact heat transfer coefficient of $100 \text{ W}/(\text{m}^2\text{K})$ was used. Both the stainless steel plate and the carbon steel substrate were meshed with tetrahedral elements. Both meshes were refined in the area with laser-metal interaction. The 316L plate had a maximum element size of 2 mm and a refinement level of 2 resulting in a total of $197\,979$ elements. The carbon steel plate had coarser maximum element size of 5 mm , but with a higher refinement level of 4 resulting in an element count of $184\,280$. An adaptive time control was used with a maximum time step of 0.03 s . Material definitions were taken from the *Simufact* Material library, and the carbon steel was approximated with DIN 1.0338. Thermodynamic Scheil solidification simulation of 316L was performed using *ThermoCalc 2022a* with the *TCFE12* database.

3 Results and discussion

The section is divided into several sub-sections which begin from the optimization of remelting process to understand the process behaviour (sub-Sect. 3.1) and process parameter limits using a single-track technique. The optimized parameters were used for a large-scale remelting process to test the performance (sub-Sect. 3.2). Comparisons with the CMT process were performed (sub-Sect. 3.3) with a comprehensive microstructural analysis (sub-Sect. 3.4). The hardness and nanoindentation were assessed (sub-Sect. 3.5). The corrosion results are provided and discussed in sub-Sect. 3.6. Finally, the productivity and energy efficiency of the tested processes were calculated and compared (sub-Sect. 3.7).

3.1 Optimization of laser remelting tracks

3.1.1 Experimental set (i)

It is estimated that to penetrate 1.0 mm of steel, 1.0 kW laser power is required at $1.0\text{--}1.5 \text{ m/min}$ welding speed [19]. However, it depends on many other factors such as the laser beam spot diameter, *FPP*, shielding gas composition/flow rate, air knife, air gap width between plates, and/or the chemical composition of base metal. Stainless steel is easier to penetrate than carbon steel due to higher absorptivity and lower thermal conductivity. Based on the preliminary testing, 4.0 kW

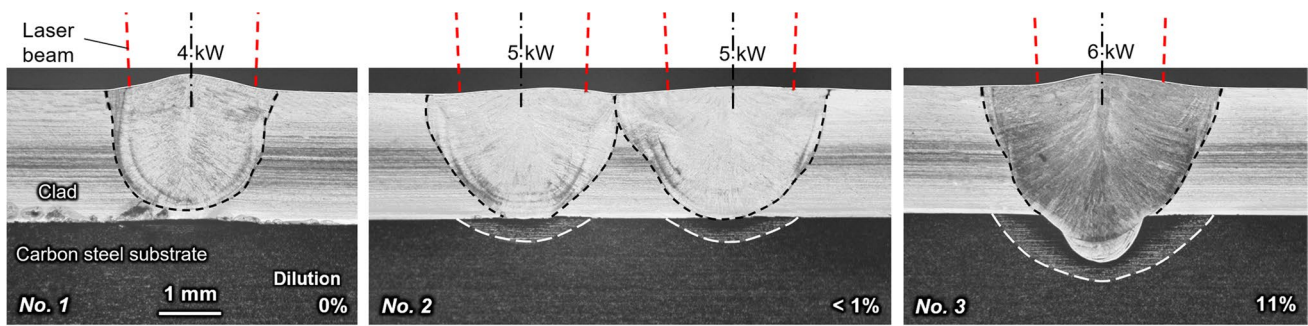


Fig. 3 Macrosections of melt tracks made at different laser beam powers with 2.0 m/min travel speed and +30 mm *FPP* of experimental set (i). Dilution values are shown in right bottom corner

at 2.0 m/min melting speeds with +30 mm *FPP* is near to achieve a full penetration of 2.0 mm thick stainless steel, see Fig. 3. With an increase up to 5.0 kW, a full penetration was achieved. At 6.0 kW, a deep penetration was achieved with 11% dilution of the base metal. Thus, 5.0–5.5 kW laser power is optimal with selected process parameters. No cracking and pores were observed. Based on the remelted track no. 2, the selected laser beam offset was too large; therefore, it was shortened in the further experimental tests. The top view of the remelted track appearance is shown in Fig. 4. At 4.0 kW laser power, there is a slight humping and undercut due to unstable melt pool related to high melting speeds at heat conduction mode. With increase of laser power to 5.0 kW, a more consistent quality was achieved with wider melt pool. At 6.0 kW, there is a transition towards the keyhole processing based on the fusion zone geometry. Therefore, processing is more stable at such high melting speeds, but it has increased dilution due to the keyhole formation which starts to penetrate deeply into the carbon steel substrate.

3.1.2 Experimental set (ii)

The experimental set (ii) was performed using a decreased travel speed of the laser beam to 1.5 m/min to avoid humping and undercut issues. Based on the macrographs (see Fig. 5), at 4.0 kW power, a full penetration with low dilution (7%) was achieved. With increased laser power to 5.0 kW, dilution was almost doubled (13%) but the melting area (between the

stainless steel plate and the substrate) was also increased. Since the welds were V-shaped, a large track overlapping is needed to reduce unmelted zones between tracks. At 6.0 kW laser, the deep keyhole provided excessive penetration with high dilution (28%) and some porosity. The top view appearance of the tracks showed a good quality with all used laser powers, see Fig. 6.

3.1.3 Experimental set (iii) and (iv)

An increase in *FPP* (+60 mm) provided almost twofold larger spot diameter. Therefore, to achieve a full penetration, the laser power was increased at 1.5 m/min travel speed, see the experimental set (iii). The lack of penetration was achieved within the range of 6.0–9.0 kW beam power. Henceforth, a full penetration was achieved at 10 kW with low dilution (<2%). The corresponding macrosections of the remelted tracks are shown in Fig. 7. All remelted tracks showed an unstable melt pool behaviour with humping and undercut, see Fig. 8.

The larger spot size provided unstable the melt pool behaviour. No improvement in quality was achieved at slower travels speeds (1.0 m/min) using 7.0 kW laser beam power. Moreover, the undercut and humping was higher by decreasing the laser beam power to 5.0 kW. The underlying physics of unstable weld pool is very complex and there are many reasons for its occurrence, and some of them are described in the work done by Wei [20]. The upper bead



Fig. 4 Melt track appearance with 2.0 m/min travel speed and +30 mm *FPP* (no. 1–3) of experimental set (i). Note, two tracks were made with 5.0 kW to test effect of laser beam offset. The arrows show laser beam remelting direction

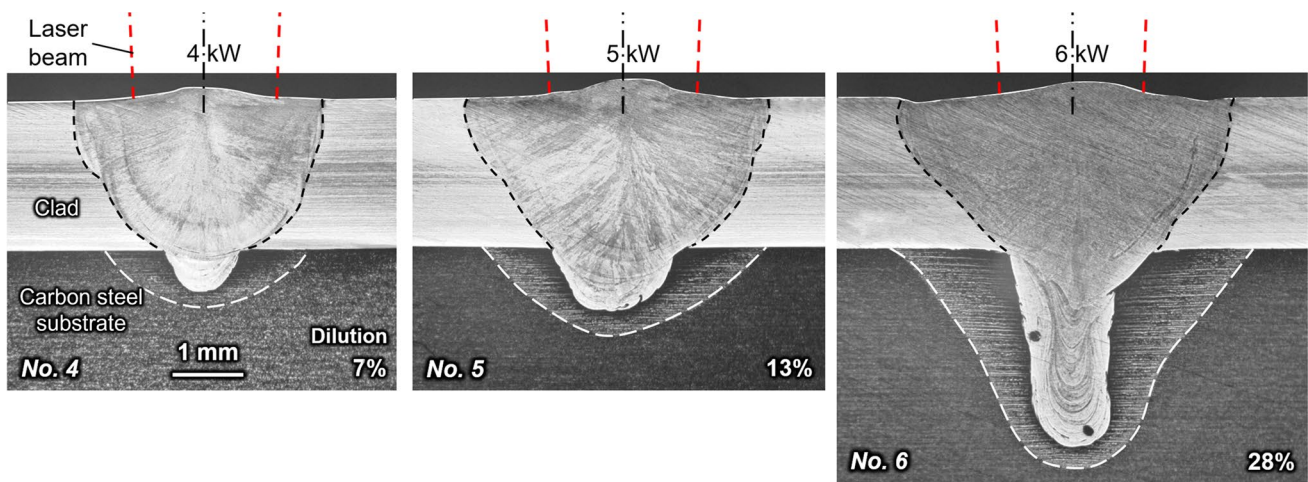


Fig. 5 Macrosections of melt tracks made with 1.5 m/min travel speed and +30 mm *FPP* of experimental set (ii). Dilution values are shown in right bottom corner

humping and other instabilities occurs at increasing welding/melting speeds due to upwards melt flows [21]. Higher laser power provided wider melt pool (liquid channel) with slower cooling rates; hence humping was lower.

3.1.4 Optimization of the remelting process

The experimental results are represented in the form of the graph (see Fig. 9) showing processing stability areas. A good quality remelt appearance with low dilution can be achieved at 1.5–2.0 m/min travel speed range within the range of 1.8–2.1 kW/mm² laser beam density. It is well-known that the transition from the heat conduction to the keyhole mode is at ~ 1.0 MW/cm² or ~ 10 kW/mm² and it can vary depending on numerous factors which are: thermo-physical properties of a material, reflectivity conditions or surface quality of specimen, laser wavelength, and process parameters. Therefore, the keyholing regime for a stainless steel is assumed to have a threshold in the range of 0.5–1.0 MW/cm² or 5–10 kW/mm² [22]. As a result, the conducted experiments at +30 mm *FPP* had a transition behaviour, whereas the heat conduction mode was predominant for +60 mm *FPP*. The defocused laser beam at +60 mm *FPP* did not provide a

stable melt pool at any parameters. Therefore, the average laser beam density parameter does not reflect the stability of processing. In this case, the *FPP* or the beam diameter should be indicated. However, beam spot diameter has limits since a more focused laser beam (having a smaller spot diameter) provides smaller melt pool; thus, productivity is decreased. More defocused laser beam spot at +60 mm *FPP* may not provide any benefits due to excessive heat input and unstable melt pool is of high risk.

The laser beam remelting produced a typical V-shaped remelted areas or the fusion zone (see Fig. 10a). This is more pronounced with the focused laser beam. The shape of the fusion zone can be manipulated but is restricted for cladding since it requires a partial penetration with minimization of dilution. In contrast, in laser beam welding under a full penetration regime, a straight fusion zone can be easily achieved. For cladding purposes, such shape of the remelted areas may cause issues between the tracks where some areas are not melted. These areas reduce metallurgical bonding and should be avoided in clads where high mechanical properties are required. For higher productivity, it is beneficial to use a slightly defocused laser to remelt higher volume of the cladding metal, see Fig. 10b. However, it is highly probable



Fig. 6 Melt track appearance with 1.5 m/min travel speed and +30 mm *FPP* (no. 4–6) of experimental set (ii). The arrows show laser beam remelting direction

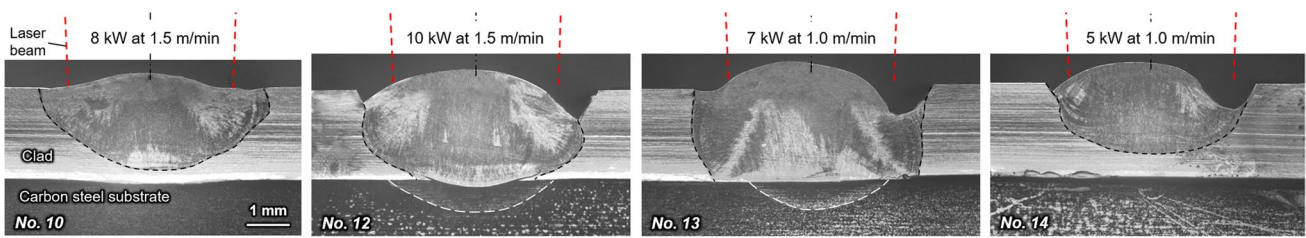


Fig. 7 Macrosections of melt tracks made +60 mm FPP from experimental set (iii) and (iv)

that the shape of fusion zone will be the same shape containing non-melted areas. A further increase in beam spot diameter to melt more metal may provide no benefits since the shape will be more hemispherical and possibly even with larger non-metal areas (see Fig. 10c). To eliminate the non-melted areas, an offset-distance between tracks should be decreased to increase overlapping. However, it will reduce the efficiency of processing by remelting of a significant area of the previously deposited neighbour fusion zones. Furthermore, it also provides much higher heat input. Therefore, the overlapping values should be optimized which requires additional experimental testing and modelling. In this case, a possible alternative is to apply laser beam oscillations. In this way, the melt pool will be much wider and the corners accumulate more heat due to higher accumulated power

density [23]. Here, in addition to oscillation parameters, the optimization of the laser beam offset distance should be also considered. With appropriate oscillation parameters and laser beam offset, full remelting of the preplaced metal plate may be achieved. Another possible alternative is (i) to use a non-Gaussian beam shape such as top-hat, or squared-shaped heat distribution, or (ii) multi-beam systems.

3.2 Full scale laser remelting with optimized parameters

Understanding the boundaries of the processing window for laser remelting under a strict control of dilution is of critical importance to produce acceptable quality clads repeatedly and consistently. Therefore, the optimized

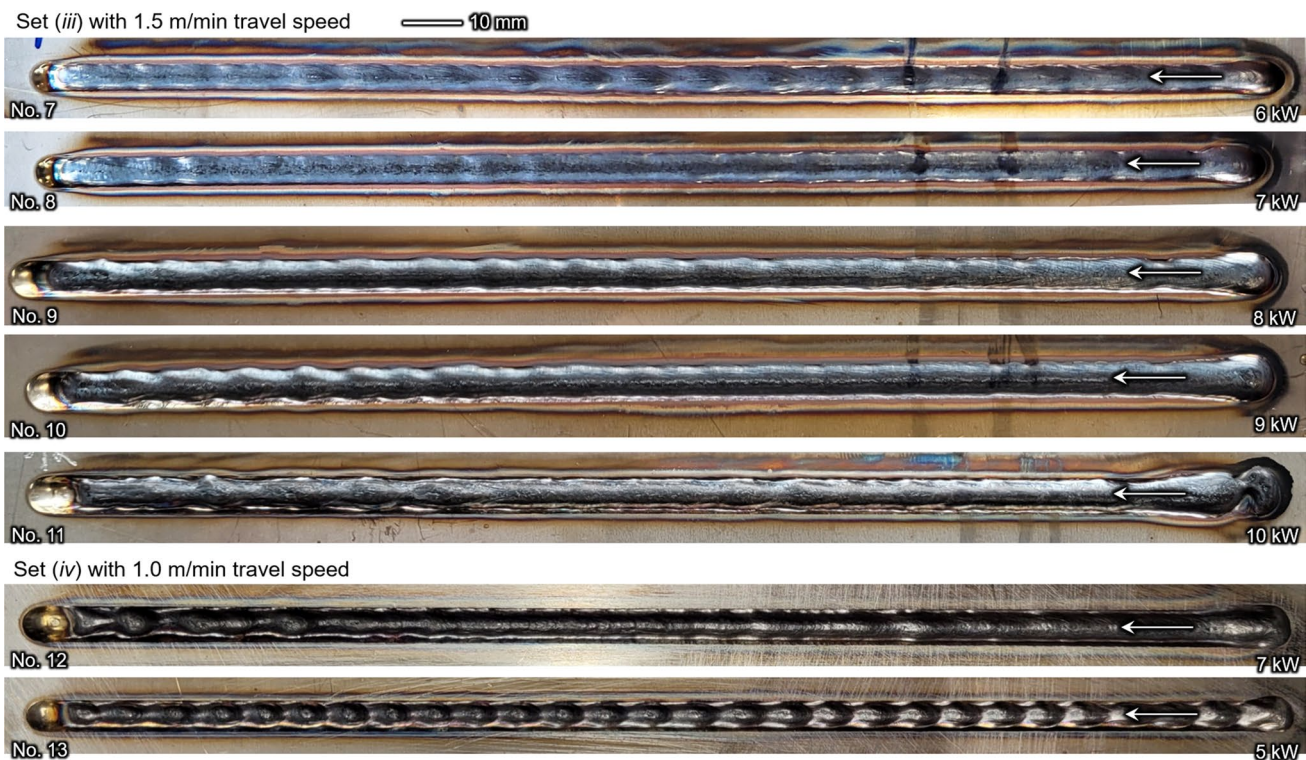


Fig. 8 Appearances of laser-remelted tracks of preplaced stainless steel plate on carbon steel substrate made at +60 mm FPP at different laser beam power outputs and travel speeds from experimental set (iii) and (iv). The arrows show laser beam remelting direction

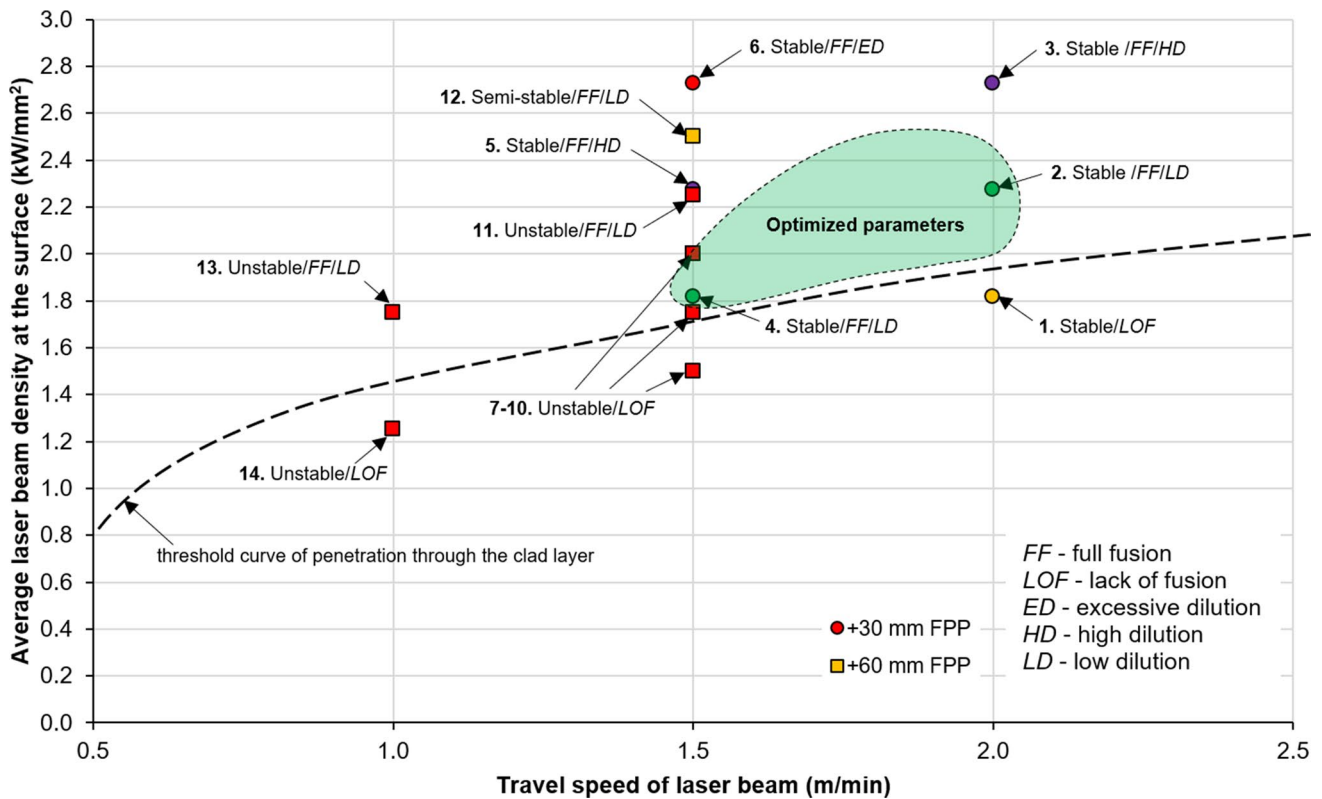


Fig. 9 Established processing map based on experimental work. Note, optimized process window is valid only for +30 mm FPP

parameters which provided a full penetration and relatively low dilution (5.0–6.0 kW laser power range at 2.0 m/min melting speed and +30 mm FPP) were applied to remelt a larger area of the preplaced stainless steel plate, close to the real manufacturing conditions. When the 2.5 mm laser beam offset was used at 5.0 kW laser power, the tracks had

a poor quality with excessive humping, see Fig. 11a. Note, the remelting process was continuous without any delays in remelting of the subsequent track. Such unstable behaviour of the melt pool was absent for the one-track cases. In the multi-track cases, there is an unstable remelting of the adjacent previously deposited track with uneven surface

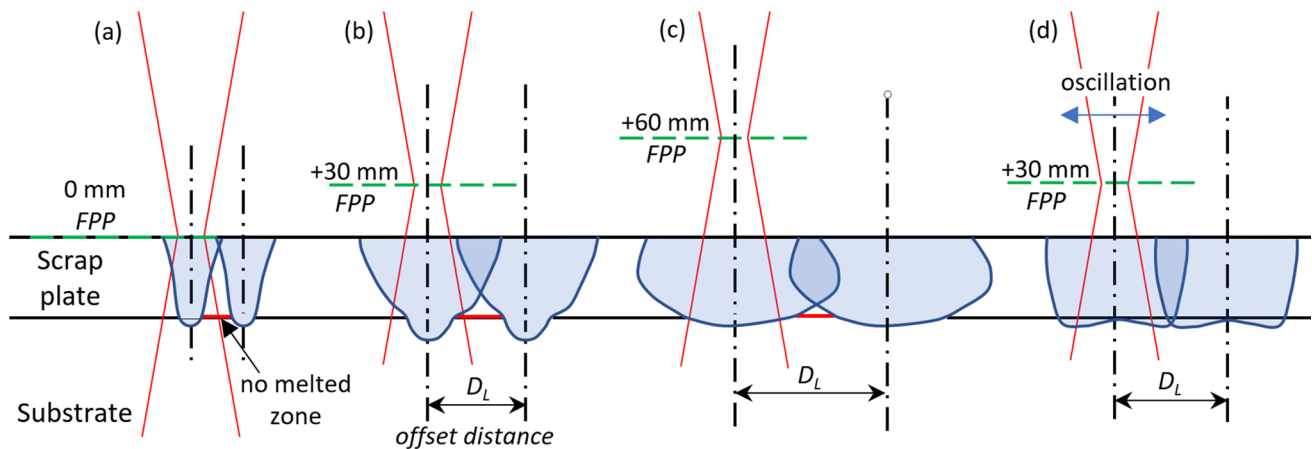


Fig. 10 Issues of remelting track geometry and consequences on quality: **a** typical weld geometry and possible issues with low productivity, **b** optimization of tracks by defocused laser beam and offset

distance of laser beam. **c** highly defocused laser beam and **d** proposed laser beam oscillations for improved quality and productivity

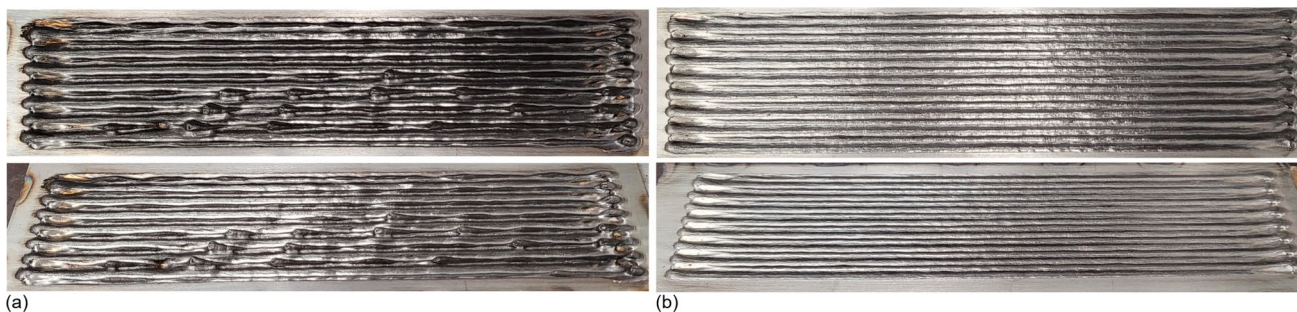


Fig. 11 Large-scale multi-melt track appearance of **a** 5.0 kW laser power at 2.0 m/min melting speed (remelt track no. 14), and **b** 6.0 kW laser power (remelt track no. 15). Melting speed of 2.0 m/min melting

speed at +30 mm *FPP*. Perpendicular view on top picture and angled view at the bottom. The length of the remelted tracks is ~125 mm

compared to the flat non-melted preplaced plate. Using 6.0 kW laser power, the high-quality remelted tracks were made at all laser beam offsets as well as with 5.5 kW laser power, see Fig. 11b. Such trend was noted with +60 mm *FPP* cases, where lower laser beam power provided more unstable conditions (see Fig. 7). The use of lower remelting speeds and powers provided more stable remelt pool and solidification conditions which may be related to slower melt flows.

The macrosections of the multi-track experiments are shown in Fig. 12. The experiment no. 14 had a consistent offset distance of the laser beam with a periodic variation in penetration depth which may be related to the laser axis angle, which is dragging or pushing. However, an inconsistent laser beam offset was noted with higher laser

powers (5.5–6.0 kW) and shorter offset distances. After every second track a slightly larger offset was generated, denoted as the near-distance and the far-distance offset. It is important to note that the multiple track remelting process is more complex since with each subsequently deposited track, the conditions are slightly different. For example, the temperature of the stainless steel plate and substrate is increasing and the subsequent tracks may have higher penetration depth with increased dilution. Inconsistency in the beam offset tend to provide the non-melted zones (shown as red lines indicated by the arrows in Fig. 12). These zones should be avoided since it may provide poor mechanical properties and corrosion resistance. By using a shorter laser beam offset of 2.2 mm, the non-melted zones were slightly reduced (experiments no.

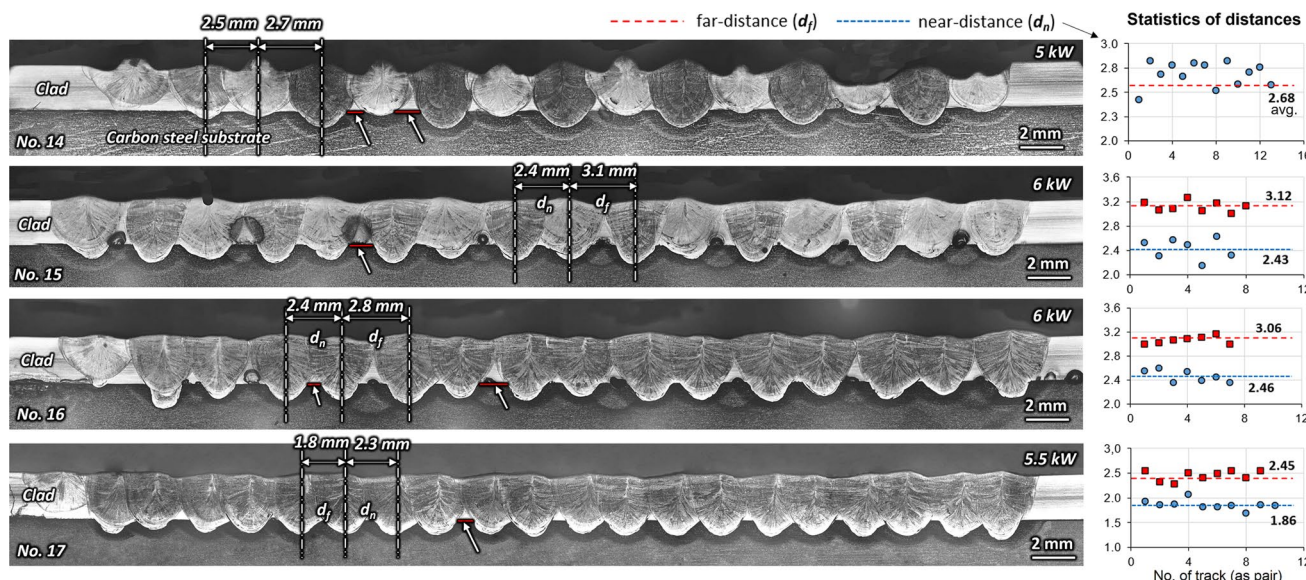


Fig. 12 Macrosections of the melt tracks made with 2.0 m/min melting speed and +60 mm *FPP* of experimental set (v) shown on the left. Lack of fusions are shown with the arrows. Statistics of distances

shown on the right where x-axis shows the number of tracks and y-axis is the distance between the tracks

15–16). In addition, 6.0 kW laser beam power provided higher dilution (~25%) and can be reduced by a slightly decreasing laser power. A further decrease in the laser beam offset to 1.8 mm and laser power to 5.5 kW (experiment no. 17), improved the overlapping of the tracks and reduced dilution.

3.3 Conventional CMT arc cladding compared with laser remelting

The conventional CMT arc cladding is simpler than laser beam remelting due to fewer process parameters and well-established synergy lines. After a few trials, a good quality clads were achieved using 9.0 mm/s (or 0.54 m/min) travel speed with 122 A/22.2 V corresponding to 4.7 m/min wire feed speed, see Fig. 13a. Laser remelting of the pre-placed plate with optimized parameters (experiment no. 17) is shown in Fig. 13b. Both methods provided a good appearance of the tracks without spatter, cracking nor surface pores. The average height was 2.3–2.5 mm produced by CMT, which is slightly higher than laser remelting of plate. CMT cladding has limits in depositing thinner tracks than 2 mm; thus, the laser remelting provides much higher accuracy of the height control, but it depends fully on chosen plate thickness. Dilution was similar for both processes, 17.2% for the CMT cladding and 16.1% for the laser remelting. Therefore, the direct comparisons can be made. Notably, both processes may provide lower dilution with further refined optimization. The laser remelting may have much higher potential since laser beam is more flexible and precise tool; henceforth, dilution may be < 5% by using top-hat heat distribution profile and/or laser beam oscillation (as discussed in sub-Sect. 3.1.4).

3.4 Microstructural study

An important feature of a clad is the intermediate layer produced as the partially mixed zone near HAZ. The CMT cladding provided the intermediate layer in thickness of 13–18 μm compared to 5.0–8.0 μm obtained by the laser remelting. In the latter case, the intermediate layer was more discontinuous with sharper edges through dendritic growth direction. For improved corrosion resistance, this layer should be as small as possible; henceforth, laser remelting may have higher corrosion resistance in this area.

The gradient change in chemical composition along the intermediate layer based on EDS data is shown in Fig. 14. A sharp decrease of the main alloying elements (Cr, Ni, Mo) is observed within the intermediate layer towards the HAZ. Some high peaks in concentration of Cr and Mo were observed near the intermediate layer in the root area in the CMT clads. Therefore, Cr and Mo carbides ($M_{23}C_6$) are expected. The average Cr content (wt.%) within the clad layers was reduced by 14.0% (by percentage not wt.%) compared to the parent ASST plate and the wire in case of CMT clad. Since dilution with carbon steel was 17.2%, this explains the content of the Cr in the clad layer. The average Ni content (wt.%) was reduced by 30% (by percentage not wt.%). However, it showed higher variation; thus, the EDS points located outside the austenite-rich dendrites had lower content. Another factor could be a high degree of Ni macrosegregation. The similar trend as Ni showed Mo content, which was also reduced by 27% with macrosegregation. Cr and Ni content for the laser remelting was similar to the CMT cladding but the alloy elements were slightly reduced having a similar dilution. Owing that Cr and Ni have relatively low boiling points (2672°C and 2730°C respectively), they may slightly evaporate due to high temperatures found

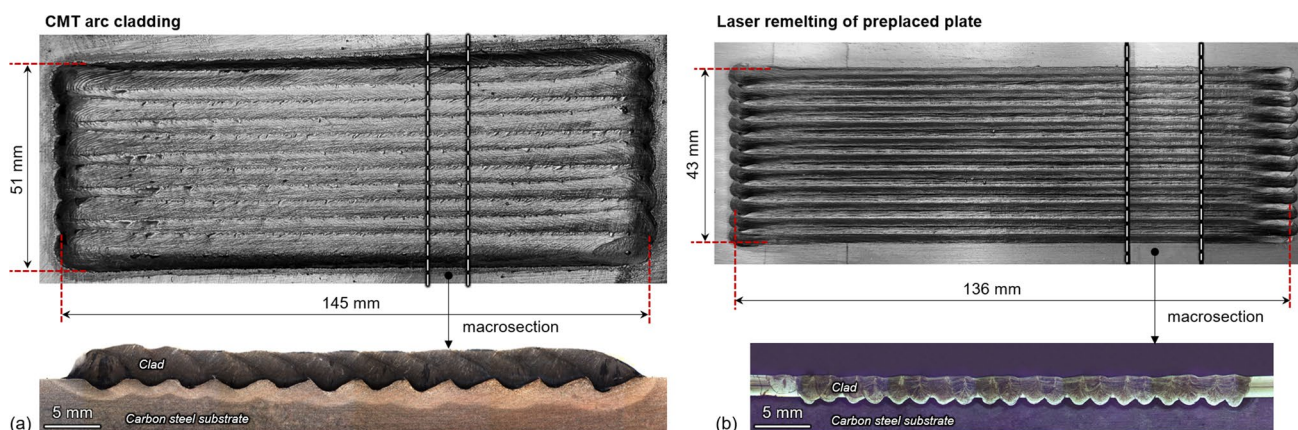


Fig. 13 Outlook of clad tracks and their macrosections made with **a** conventional CMT arc cladding process and **b** laser remelting of preplaced plate

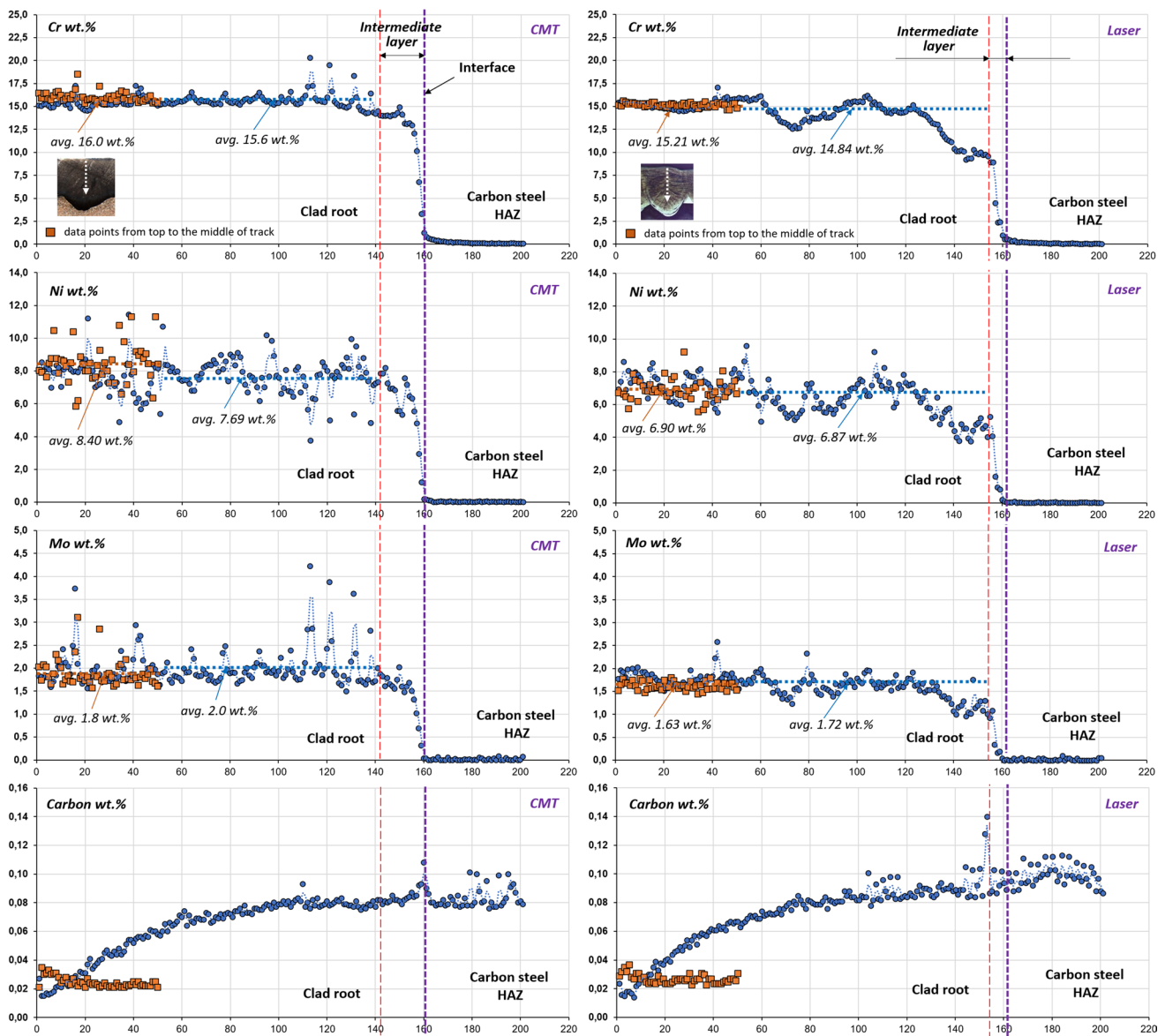


Fig. 14 Chemical composition (based on EDS data) along the intermediate layer (consisting of 200 measured points with interdistance of 1.0 μm) and from top to middle of clad layer (consisting of 50

points with interdistance of 25 μm) for CMT (on the left) and laser cladding (on the right). Avg. means the average values

in the quasi-keyhole mode. The difference in chemical composition in the root and the middle of the remelted tracks marginal. This means that both CMT and laser processes had a finely homogenous mixing of elements. Since both processes provided more than 10.5 wt.% of Cr, a high corrosion resistance is expected.

The high peaks of carbon content are more notable for the laser induced intermediate layer which is related to the fast cooling rates. Therefore, a higher hardness is expected in these areas. Based on Fig. 14, the intermediate layer is carburized according to carbon diffusion from the substrate which follows the Fick’s Second Law of diffusion with

relation to an Arrhenius-type equation due to kinetics and dependence on temperature [24]. The thickness of the carburization shows almost identical values for both processes (130–140 μm), although the cooling time is much faster for the laser remelting case. Therefore, there are factors indicating that a higher diffusion rate in the laser remelting is related to the higher peak temperatures provided by the keyhole. This may influence the activation energy. No decarburization was found in the HAZ for both cases which is related to the fast cooling times, especially for the LBW remelting, to prevent excessive carbon diffusion. Decarburization has been reported by many researchers and it is considered as negative

phenomenon since it lowers the hardness, consequently the strength may be reduced. Use of pure nickel interlayer is common to eliminate the decarburization by introducing a barrier for carbon diffusion. Lin et al. [25] showed a decarburized-free layer near the interface by using 100–200 μm pure Ni interlayer in hot-rolling process which possess much slower cooling than used processes in this work.

Based on the Schaeffler diagram [26], the microstructures for both processes tend to be fully austenitic with 2–3% of delta ferrite when initial chemical composition is assumed, see in Fig. 15a. Based on the measured EDS points, the microstructure for CMT tend to be FA with ~10% of delta ferrite close to the martensite formation zone. The microstructure in the laser beam remelting is shown to be located within the A + M + F zone with a similar delta ferrite amount. The WRC-1992 diagram [27], showed dual F–FA (14–16% of delta ferrite) solidification mode for both cases (see Supplementary Material 1). However, the cooling rate is not implemented in these diagrams which may have a significant effect on the microstructure and solidification parameters. Another method is based on the Fe–Cr–Ni ternary diagram with 70% of iron. Based on the EDS data, it showed FA solidification mode as well (see Supplementary Material 2). Hence, the solidification sequence upon cooling is: $liquid \rightarrow liquid + \delta \rightarrow liquid + \delta + \gamma \rightarrow \delta + \gamma \rightarrow \gamma$ (for $1.5 < Cr_{eq}/Ni_{eq} < 2.0$). However, this diagram has limited accuracy since it does not incorporate the effect of other alloying elements and solidification rate.

According to the optical micrographs and SEM images shown in Fig. 16, the CMT clad layer was mainly characterized by primary austenite with the wide γ -dendrites and secondary delta ferrite microstructure, or austenitic–ferritic (FA) solidification mode. The residual δ -ferrite was estimated to be $11.0 \pm 1.0\%$ located between the γ -dendrites. The appearance of the δ -ferrite consisted of dual vermicular

(or skeletal) and lacy (or lathy) morphologies. A similar microstructure with AF solidification mode was reported by Wang et al. [28] in CMT for WAAM of 316L ASST walls where similar process parameters were used but no lacy delta ferrite was noticed. These observations are more consistent with the Schaeffler diagram.

Based on the solidification diagram proposed by Lippold [29], where the solidification rate is incorporated, the microstructure tend to be primary ferrite with Widmanstätten austenite (see Fig. 15b) based on the EDS measurements, which is inconsistent with the observed microstructure. However, if the initial chemical composition (see Table 1) values are taken with consideration of dilution, the predicted microstructure tend to be more correct. Note, the solidification rate was assumed equal to the cladding/remelting speed. Another diagram which includes the solidification velocity, proposed by Elmer et al. [30], showed a more realistic prediction of the microstructure showing AF solidification mode (see Supplementary Material 3). More equiaxed dendrites were observed on the top area of tracks and combination of the planar cells and the fine columnar dendrites near the root, which grows epitaxially (parallel to the heat extraction direction) from the solid–liquid interface.

In the laser beam remelted layer with higher cooling rate, the solidification mode tends to be primary ferrite with austenite (FA mode), according to OM and SEM images (Fig. 16). The residual δ -ferrite fraction was $12.6 \pm 0.5\%$ which is slightly higher than that obtained from the CMT, and it was characterized by a fine vermicular and lacy morphology (see Fig. 16b). Based on the previously used diagrams, it showed FA solidification mode which is consistent with the observations. However, the prediction based on the diagram with solidification rate showed to be erroneous. The predicted points tend to be located on the border between fully austenitic, AF, and F/MA (see Fig. 15b) when initial

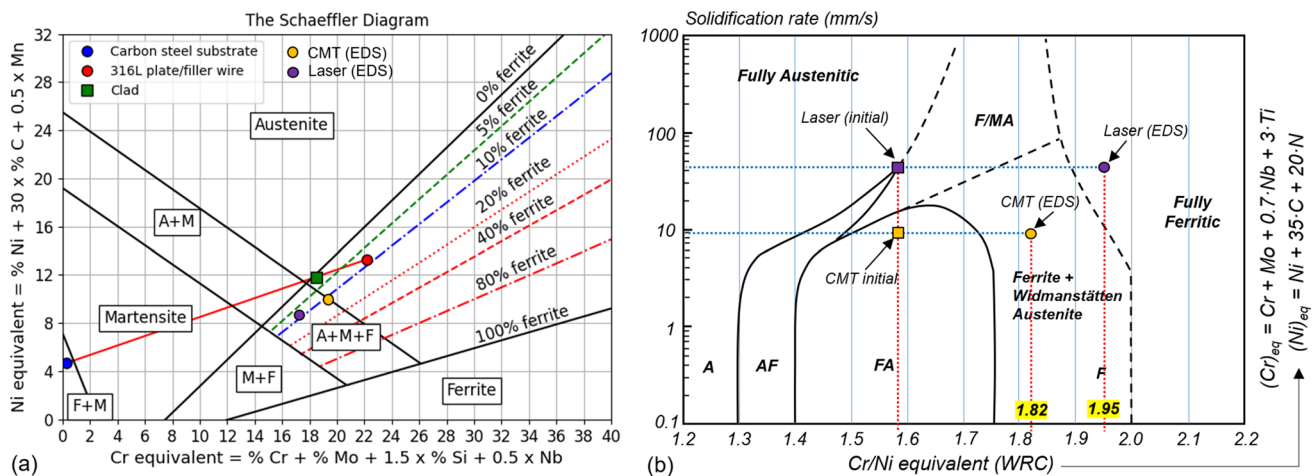


Fig. 15 **a** Prediction of clad microstructure based on the Schaeffler diagram and **b** estimation of solidification modes based on solidification rate and Cr/Ni equivalent WRC (based on Lippold [29])

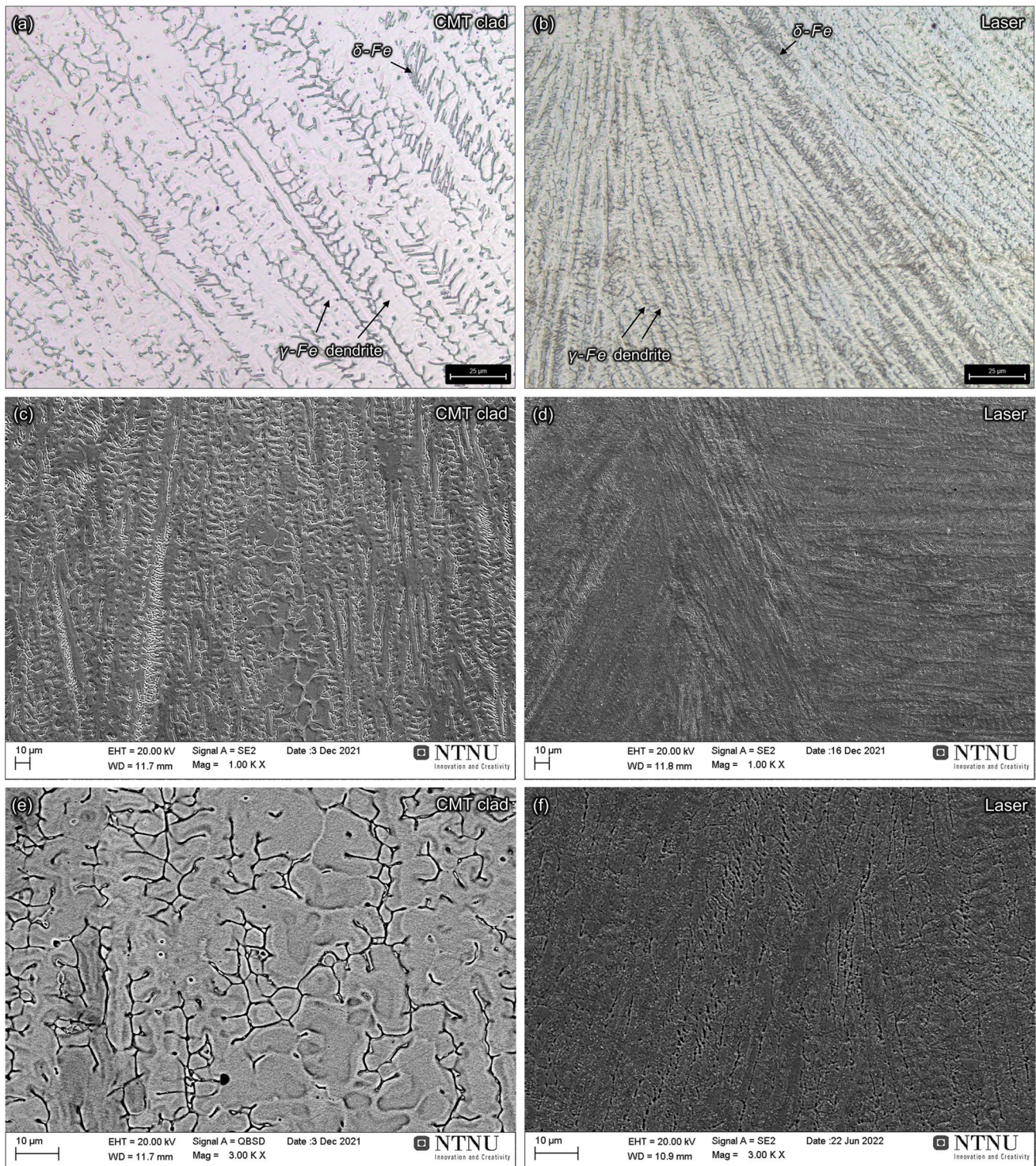


Fig. 16 Optical micrographs in the middle of bead found in **a** CMT and **b** laser-remelted clads. Scanning electron microscopy of microstructure in tracks of **c** CMT clad and **d** laser-remelted clads. High magnification SEM of **e** CMT and **f** laser-remelted clads

base values of chemical composition were taken. According to the EDS point analysis (averaged values according to Fig. 14), it showed fully ferritic solidification mode. In this case, the diagram proposed by Elmer [30] (see

Supplementary Material 3) showed more correct prediction. Note, it used pure Fe–Cr–Ni system for building the diagram; therefore, the prediction may contain some errors since the materials in this work contains other alloying elements (Mo,

Ti, Nb, etc.). Suutala [31] showed that an increase in the welding speed changed FA solidification mode towards AF when Cr_{eq}/Ni_{eq} ratio is > 1.55 due to higher growth rate under conditions of the dendritic growth. Therefore, the EDS point analysis was performed within the dendritic cores for the laser remelting case and results are presented in Table 3. Accordingly, the dendrites consisted of austenite with the residual δ -ferrite between the cores. The EDS mapping complies with these observations, with a higher Cr and Ni concentration closer towards the dendrite centreline, see Supplementary Material 4. α' -martensite formation was not observed but the laser-remelted tracks contained a higher amount of harmful $M_{23}C_6$ particles precipitated within δ -ferrite areas compared to the CMT case based on the EDS data (see Fig. 14).

Delta ferrite in low amounts within the range of 2–6% has a positive effect on the mechanical properties for austenitic stainless steels. However, an excessive volume fraction of δ -ferrite may be harmful for the toughness. According to Kamiya et al. [32], lacy δ -ferrite provided much higher toughness than vermicular δ -ferrite. Therefore, higher toughness for the laser-remelted tracks can be expected. The corrosion resistance of δ -ferrite is also reduced. Microcracks tend to develop at the $M_{23}C_6/\delta$ interface due to high strains which lowers fatigue properties as shown by Wang et al. [33]. In both cases, no sigma phase (the most deleterious for mechanical properties) was observed since the predicted microstructure tend to be located near A + M lines with low Cr equivalents. Moreover, the sigma phase formation requires much longer precipitation times (in hours). The CMT cladding process may provide advantages for the corrosion resistance and lower brittleness due to lower martensite formation. However, no cracking was observed in the laser beam remelted layers.

The primary dendritic arm spacing (PDAS, denoted as λ_1) for CMT clads was $16.7 \pm 2.8 \mu\text{m}$. Similar PDAS values were reported by Wang et al. [28] where CMT was used for WAAM of 316L ASST using similar process parameters. It is important to note that the PDAS values may differ depending on the location within the fusion zone due to rapid spatial thermal gradients. For the sake of consistency and simplicity, the measurements were taken around the centre

of the track at centreline. For the laser-remelted clads, the measured PDAS was $4.75 \pm 1.03 \mu\text{m}$ which is much smaller than for CMT due to faster cooling rates. The results are consistent with the laser beam welds of 304L by Gilath et al. [34]. Moreover, similar PDAS values were reported by Huang et al. [35] in powder-based laser cladding/AM of 316L based on the equivalently scaled heat input.

The PDAS and the cooling rate (denoted as ϵ) has a linear relationship (taken as *log*). In laser processing, the PDAS was estimated by Katayama and Matsunawa [36] for 304/310 stainless steels. Later it was confirmed by Elmer et al. [30] using different Fe–Ni–Cr steel systems and even in additive manufacturing by Huang et al. [35] in case of solidified 316L powder. The PDAS can be calculated according to the following equation:

$$\lambda_1 = 80(\epsilon)^{-0.33} \quad (2)$$

Since we know the PDAS, the cooling rate can be estimated based the following equation:

$$\epsilon_{PDAS} = \sqrt[3]{\frac{\lambda_1}{80}} \quad (3)$$

According to Eq. (3), the CMT cladding had the cooling rate of 115°C/s and the laser remelting provided 5204°C/s cooling rate which is significantly higher.

The cooling rate is directly related to welding or cladding speeds. For calculation of R (the solid–liquid interface growth rate) at the end of the melt pool where $\cos(0)$ is equal to 1, thus R can be more simplified and estimated based on the following relationship:

$$R = v_s \cos \alpha = v_s \quad (4)$$

The PDAS can be directly estimated through welding/cladding speeds (in mm/s) according to Gilath et al. [34], by the following equation:

$$\lambda_1 = 40 \cdot v_s^{-0.5} \quad (5)$$

Based on Eq. (5), the calculated PDAS for the CMT case is $\lambda_1 = 13.3 \mu\text{m}$ and for the laser remelting $\lambda_1 = 6.9 \mu\text{m}$ which

Table 3 EDS point analysis from three selected areas within the dendrite cores in the laser-remelted sample (values in wt.%) and Cr/Ni equivalent (based on the Schaeffler type). Fe balance. Carbon is taken

Point no. (location)	Ferrite stabilizing elements					Austenite stabilizing elements				Cr/Ni eq	Type of dendrite
	Cr	Mo	Si	Nb	Ti	Ni	C	Mn	Cu		
1 (dendrite core)	13.36	1.41	0.34	-	-	8.80	0.025	1.81	1.48	1.46 (15.28/10.46)	Austenite (+ martensite)
2 (dendrite core)	13.85	1.61	0.34	-	0.005	8.29	0.025	1.76	1.44	1.61 (15.97/9.92)	Austenite (+ martensite)
3 (dendrite core)	13.37	1.31	0.27	-	0.002	8.89	0.025	1.73	1.50	1.44 (15.09/10.51)	Austenite (+ martensite)

as average from Fig. 14. Type of dendrite was based on the Schaeffler diagram (Fig. 15a)

is in a good compliance with the measured experimental values of $16.7 \pm 2.8 \mu\text{m}$ and $6.26 \pm 0.61 \mu\text{m}$ respectively.

The secondary dendritic arms spacing (SDAS) measured for the CMT was $\lambda_2 = 6.26 \pm 0.61 \mu\text{m}$. A slightly larger SDAS (9–11 μm) in CMT for WAAM was reported by Wang et al. [28] and difference can be due to a special pulse used which may affect the cooling condition without dilution. Narrow dendrites in the laser remelting were measured and had very small SDAS of $\lambda = 2.29 \pm 0.75 \mu\text{m}$. It was shown in [37] that smaller SDAS increase yield strength of the fusion zone in 20 mm deep electron beam welds of 316L. The SDAS can be calculated according to the following equation [30]:

$$\lambda_2 = 25(\epsilon)^{-0.28} \tag{6}$$

Subsequently, the cooling rate for the SDAS can be estimated based the following equation:

$$\epsilon_{SDAS} = \sqrt[3]{\frac{\lambda_2}{25}} \tag{7}$$

Based on Eq. (7), the following calculated cooling rate values obtained: $\epsilon_{CMT} = 140^\circ\text{C/s}$ and $\epsilon_{laser} = 5099^\circ\text{C/s}$. These values are similar to the values based on the PDAS calculation which was based on Eq. (2). Comparing the estimated values of PDAS and SDAS (which should be equal), a marginal discrepancy in the values can be due to: (i) differences in chemical composition and its change during welding with consideration of dilution; (ii) the correct measurement of λ_2 is intricate because it changes significantly in tracks due to rapid spatial thermal gradients especially for laser-remelted case; and/or (iii) the formula is not adapted for the studied metallic alloy.

Numerical modelling was used to estimate the cooling rate (was calculated based on Eq. 3) for the laser remelting conditions of remelting track no. 18. The welding parameters of 5.5 kW at 2 m/min were used and the laser beam trajectories were parallel with a zig-zag pattern and a spacing of 1.8 mm. The normal vector of the heat source was oriented at 7° , matching the experimental setup. The Scheil solidification simulation was performed to estimate the solidification temperature range. The solidification path (see Fig. 17a) indicates that the final eutectic reaction occurs at a high solid fraction at temperature below 1350°C . The dendrite growth is therefore assumed to occur between 1450 and 1350°C and the cooling rate is extracted between these temperatures. The numerical simulation results are shown in Fig. 17b. The fusion zone geometry and the boundaries of HAZ are in a good agreement with the experimental micrograph. The peak temperature distribution in a cross section of the numerical simulation is superimposed on the experimental results. The cooling rate is extracted at five different heights within the centre of the laser trajectory (dashed line) for the 7th remelting track with 0.5 mm distance between each point. The cooling rate near the root of the melt pool, where the PDAS was measured, is 3986°C/s confirming that the PDAS approach provides a reasonable estimate for the cooling rate. The calculated cooling rates from PDAS for the laser-remelted track are visually illustrated in Fig. 18. The numerically predicted cooling rates are similar to the empirically estimated average values at the lower boundary. The measurements of PDAS were taken closer the root near the centreline where cooling rates are faster. The slight discrepancy between the measured and the numerically estimated values can be due to several reasons: (i)

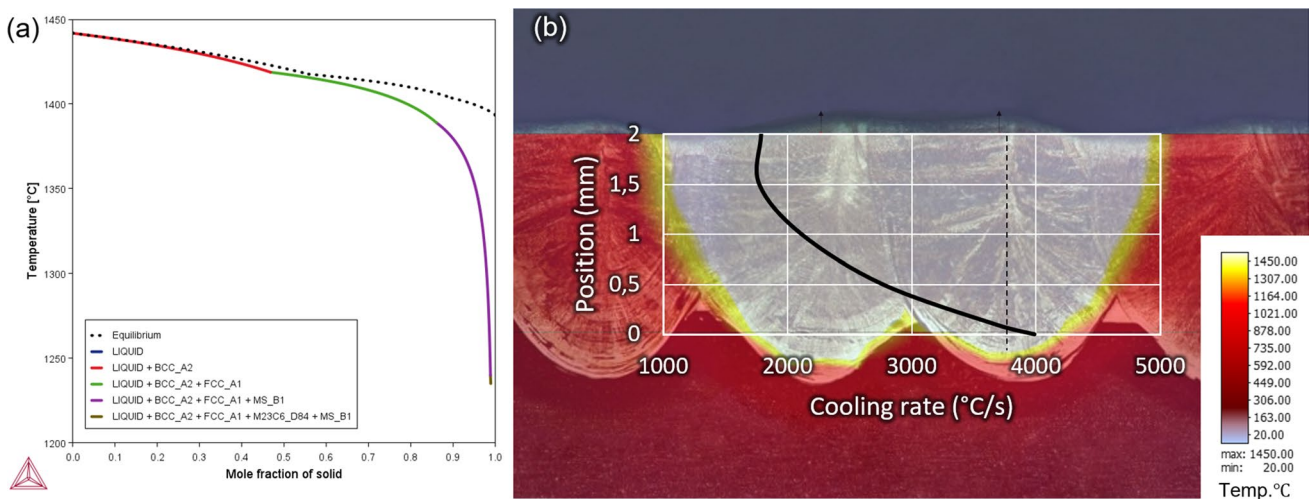


Fig. 17 **a** Scheil solidification simulation of 316L. **b** Numerical estimated thermal field overlaid on remelted tracks for laser remelting process where the cooling rate at different locations along the centreline of the melt pool is superimposed

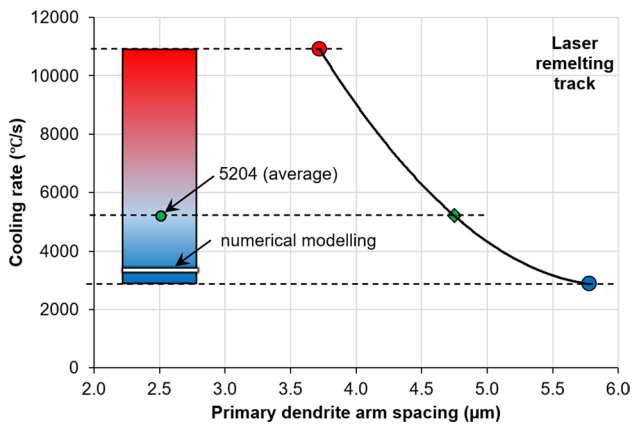


Fig. 18 Comparison of estimated cooling rate from PDAS (Eq. 3) with numerical simulation results for laser remelting track in middle of remelted bead

carbon steel dilution may influence thermo-physical properties; (ii) some inaccuracy in measurements of PDAS; (iii) modelling inaccuracies (e.g., boundary conditions); and/or (iv) simplification of the numerical model for the sake of faster calculation times. The method provides a good relevance and reliability in prediction of the cooling rates based on PDAS and vice versa. Numerical estimation of the cooling rate for CMT was not prioritized in this study due to its complex nature, which may require implementation of advanced element activation or computational fluid dynamics, since the metal is transferred in small portions with high frequencies [38].

The heat-affected zone (HAZ) for both methods was predominantly consisting of lath martensite and upper bainite due to low heat inputs and fast cooling rates. No cracking was observed in these zones. The HAZ of CMT cladding was slightly wider than laser-remelted cladding due to higher heat inputs.

3.5 Mechanical properties

Microhardness obtained from indentations at 25 gf and 200 gf loads and their comparisons are shown in Fig. 19a, b for the CMT and the laser-remelted clad respectively. The microhardness indentations were taken from the tracks closer to the middle of cladding. The hardness was higher near the intermediate layer in the case of CMT. The highest hardness can only be measured using smaller 25 gf load due to smaller indentation which may capture the narrow zones as darker bands according to the optical micrographs, see Fig. 20. These zones were inspected with SEM near the intermediate layer close to HAZ (Fig. 21a, b). High-magnification imaging inside the island-like zone revealed auto-tempered martensite and are shown to reach up to 450 HV in hardness (see Fig. 21c) as found in low carbon steel laser welds. Such conclusions are in good agreement with the EDS mapping and the point analysis, showing a similar chemical composition of such zones with the low carbon steel substrate. The existence of the low alloyed islands amidst highly alloyed stainless steel, signify that the inspected area is the partially mixed zone. Using larger hardness measurement force (200 gf) shows much lower hardness at intermediate layer due to larger indent size which covers also softer zones, where the laser-remelted tracks were chosen as an example. In general, the laser remelting provided higher hardness in average in most areas including the clad due to faster cooling rates. However, no significant difference was found in the coarse-grained HAZ.

The hardness profile obtained across the clad by nanoindentation, the intermediate layer, and the HAZ are shown in Fig. 22a and b for tests across CMT and laser clad respectively, with the corresponding average load–displacement curves shown in (c) and (d) respectively. In general, hardness is higher in the laser-cladded sample as expected.

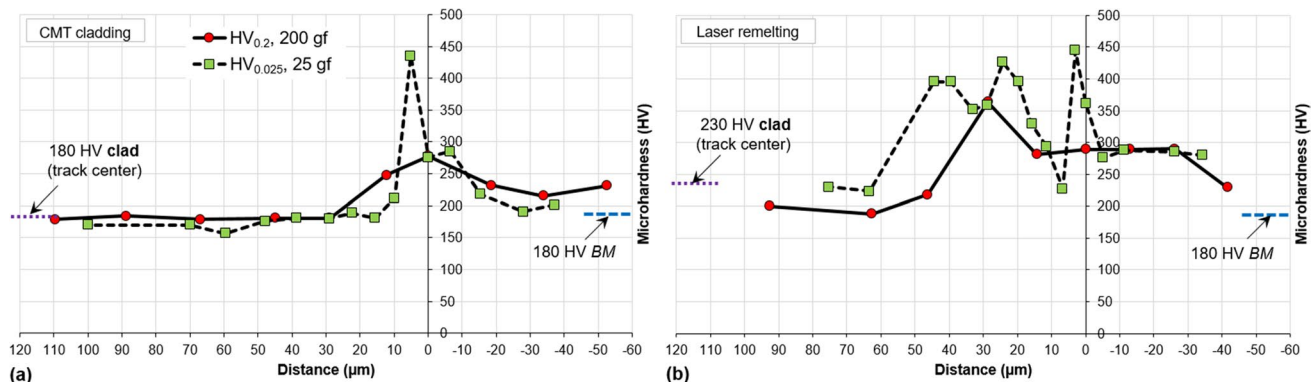


Fig. 19 Microhardness results of **a** CMT clad and **b** laser-remelted clad. Distance indicates the distance from the fusion line between intermediate layer and HAZ in the base metal

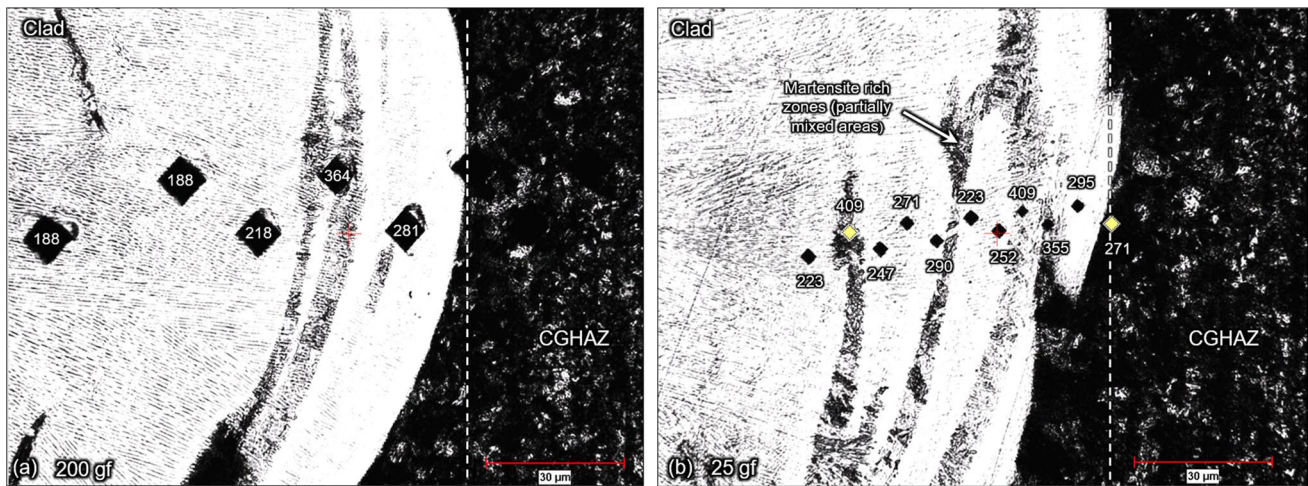


Fig. 20 Location of microhardness indents in the laser-remelted tracks using **a** larger loads=200 gf and **b** lower loads=25 gf. CGHAZ is coarse-grained heat-affected zone

Additionally, hardness peaks occurred from the partially mixed zones between the remelted tracks, in agreement with micro-indentation. According to the values presented in Fig. 22, the hardness values by recalculating from GPa to HV according to the following formula $94.5 \times \text{GPa}$ (based on ISO 14577–1) are in a good agreement with the values obtained from the microhardness tests (25 gf) and show a comparable hardness trend related to the microstructural features and morphology, see Fig. 19. Qian et al. [39] showed that a typical hardness obtained for stainless steel (304 type) using 0.5 mN load is about 5–6 GPa, which is consistent

with the peak values obtained in this work. Similar peak values were found in the work done by Murkute et al. [40] using 316L as clad material even though their case was operating under much faster cooling rates and a loading was significantly larger (150 mN). However, higher hardness was measured in the clad ~285 HV which is higher by 58% compared to the microhardness values. It is well known that nanoindentation provides higher values, in the range of 10–30%, compared to microhardness HV test (depending on the indentation load) and referred to as the size effect, explicitly showed in [39]. The hardness value depends on

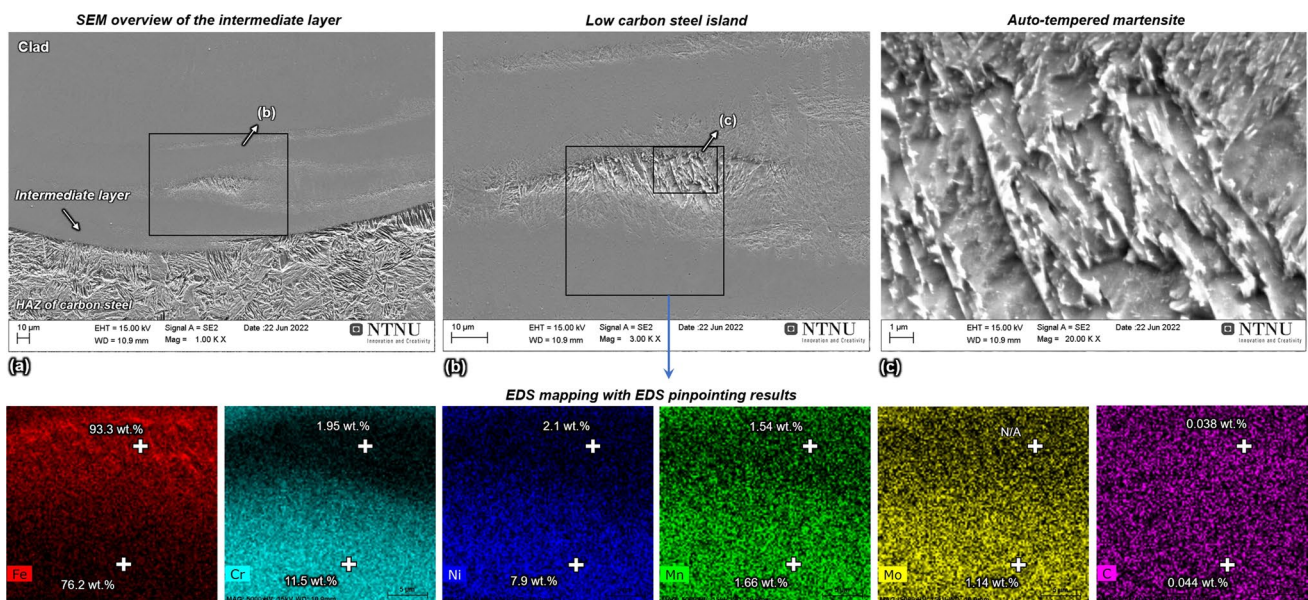


Fig. 21 SEM images at **a** near intermediate layer, **b** non-alloyed islands with **c** auto-tempered martensite and EDS mapping of chemical elements (wt.%) with point analysis of areas of interest in laser-remelted track

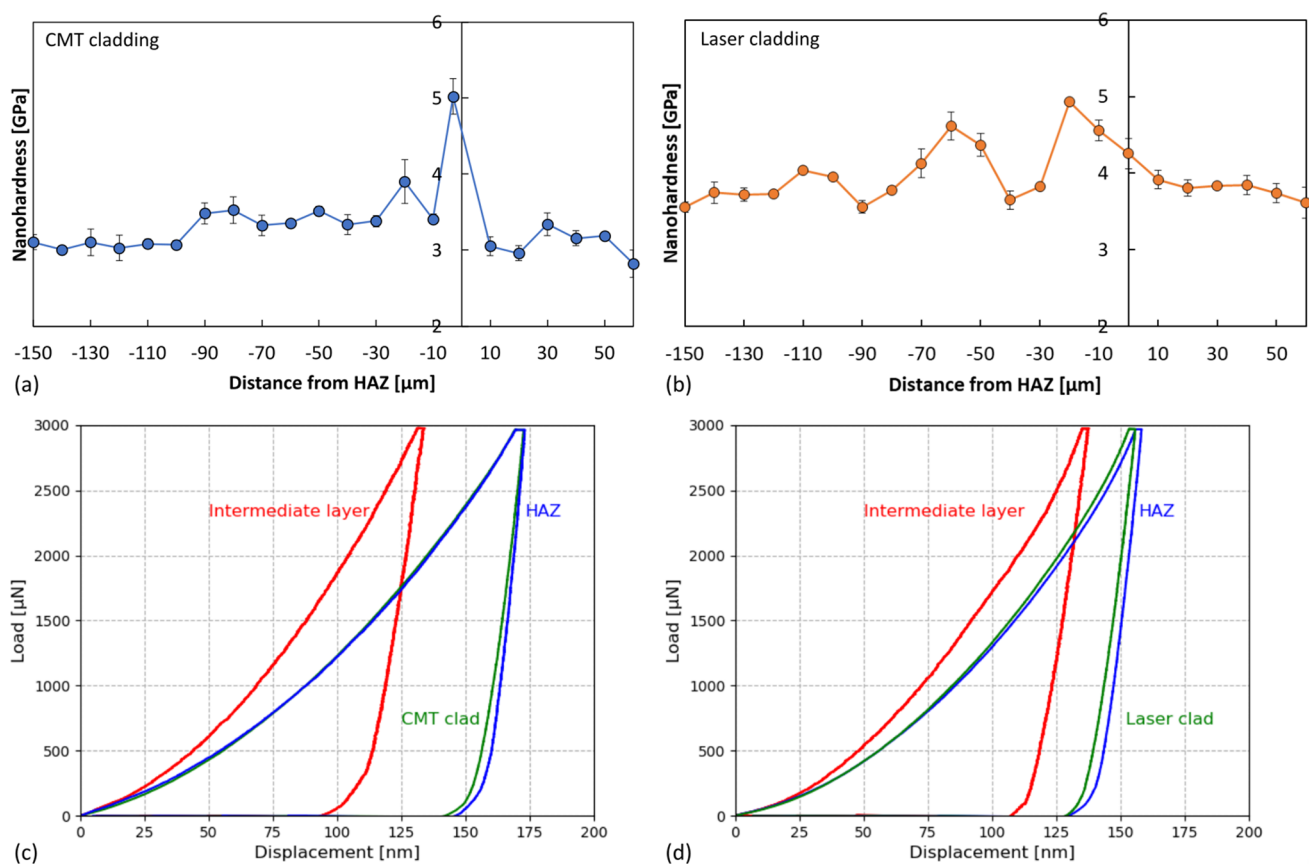


Fig. 22 Hardness profile from nanoindentation across clad, intermediate zone, and HAZ on the **a** CMT and **b** laser-clad specimens with the corresponding load–displacement curves in **c** and **d**, respectively

the indentation depth and increases with lower indentation depth. Therefore, tip geometry and indentation depth (and load) should be given with hardness data. For crystalline metals, the size effect is dominated by the dislocation-based mechanisms, resulting in a hardening effect. In addition, scatter in hardness results may occur due to the possibility of indenting other microstructural features in the inhomogeneous microstructure, such as the interdendritic area or cementite in HAZ. The inhomogeneity of the microstructure is also clearly reflected in the recorded load–displacement data from the nano-indentations, by means of lower indentation depth in the harder zones, shown in Fig. 22c and d for the CMT and laser clad, respectively. According to the nanoindentation results, it is expected to have a higher wear resistance for the clad layer made by the laser remelting case, but ductility may be lower, whereas the intermediate layer showed similar hardness values, although the laser remelting process had a thinner intermediate layer than CMT overall and it had higher hardness in the clad due to faster cooling rates; thus, harder phases and unmixed zones (Fig. 20b) were found near the intermediate layer. As a result, micro- and nano-hardness showed longer continuation of the peak hardness as reflected in both Figs. 19 and 22.

3.6 Corrosion testing

The corrosion potential E_{corr} or open circuit potential E_{ocp} was recorded for the 316L SS samples, the CMT clad samples and those obtained by the laser remelting process. The time dependences of for different samples in 3.5 wt.% NaCl are presented in Fig. 23 where the E_{ocp} curves for the two baseline 316L SS samples exhibited high E_{ocp} (more positive than -0.1 V vs. Ag/AgCl) that increased further with time due to the formation of a corrosion-resistant chromium oxide surface film. Furthermore, the time dependency of E_{ocp} on 316L SS shows the presence of occasional transients confirming the occurrence of pitting corrosion. E_{ocp} measurements on clad samples showed slight fluctuations over the narrow potential range, indicating the stability and linearity of the investigated samples. E_{ocp} of the 316L SS samples shown the most positive value followed by the E_{ocp} value of samples obtained by laser remelting process, while the samples obtained by the CMT arc cladding exhibited the most negative potentials. Since E_{ocp} is the measure of corrosion susceptibility, the shift in E_{ocp} to more positive values indicate that the sample obtained by the laser remelting process should exhibit

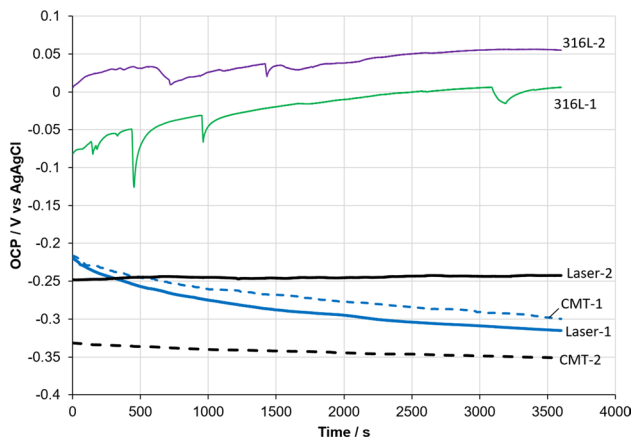


Fig. 23 Open-circuit potential, E_{ocp} , as a function of exposure time in 3.5 wt.% NaCl for 316L plate, CMT clad, and laser remelting clad

higher corrosion stability than the samples obtained by CMT arc cladding. Following the E_{ocp} measurements, the LPR tests were performed, and the value of polarization resistance (R_p) was calculated as the slope of the linear portion of voltage-versus-current curve of the LPR around the E_{corr} value. PDS measurements were performed to obtain the polarization curves. Corrosion current densities were determined using Tafel analysis. Figure 24 illustrates the polarization curves for 316L SS and the clad samples in 3.5 wt.% NaCl. In the case of polarization curves for 316L SS, cathodic curve produces a longer and better defined Tafel region, while the anodic polarization curves show passivation and pitting occurrence. The cathodic Tafel region is extrapolated back to zero overvoltage to give the net rate of the cathodic reaction at the corrosion potential, i.e. corrosion current density, j_{corr} . On the other hand, polarization curves for the CMT and laser clads have a longer and better defined anodic Tafel region, while the

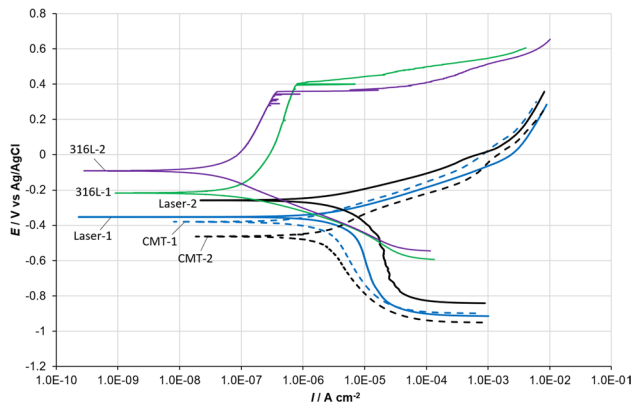


Fig. 24 Polarization curves for 316L plate, CMT clad, and laser remelting clad in 3.5 wt. % NaCl solution

cathodic polarization curves show oxygen reduction limiting current. The 316L SS samples shown distinct pitting potentials, while for the clad samples, the pitting potential was not detected. The values of polarization resistance, R_p , corrosion current density (j_{corr}) for 316L SS steel, samples obtained by the CMT arc cladding and those obtained by laser remelting process are given in Table 4. R_p is the polarization resistance determined from the slope of the potential versus current density curve over the narrow potential range of -20 to $+20$ mV relative to the corrosion potential.

From the polarization curves in Fig. 24 and data in Table 4, a shift in the E_{corr} towards more noble values for the laser remelting clad is apparent compared to the CMT clad. Furthermore, the laser remelting clads showed somewhat lower anodic current density, slightly lower j_{corr} as well as the increase in R_p . This indicates that the laser remelting clad has slightly better corrosion properties compared to CMT clad. The j_{corr} and R_p values from clad-ded samples are comparable to that previously reported in the literature for the stainless steel clads on carbon steel obtained using powder bed fusion-selective laser melting [40]. The difference in the corrosion behaviour of the 316L plates and clads can be correlated with the chromium content, microstructural differences, and surface roughness [40]. The weakening of the corrosion resistance on clads compared to 316L SS can be explained by the interdiffusion between the two materials that occurs during welding, which increases the C content, and decreases the Cr content in the 316L. Furthermore, 316L SS specimens had highly polished surfaces, reducing the number of pit nucleation, while the clad surfaces had higher surface roughness leading to lower pitting potential [41]. In addition, the formation of δ -ferrite lowers the concentrations of Cr and Mo in the γ phase and consequently degrades the corrosion resistance of the austenitic stainless steel.

Table 4 Corrosion parameters obtained from LPR and PDS measurements for 316L stainless steel, samples obtained by CMT arc cladding and those obtained by laser remelting process in 3.5 wt.% NaCl

Sample	E_{corr} /mV vs Ag/AgCl	$j_{corr}/\mu\text{Acm}^{-2}$ (from Tafel curves)	$R_p/\text{k}\Omega\text{cm}^2$ (from LPR)
Plate 316L-2	-90	$7.00 \cdot 10^{-2}$	1632.8
Plate 316L-1	-215	$2.04 \cdot 10^{-2}$	1475.8
Laser-2	-255	1.67	10.74
Laser-1	-354	1.98	6.60
CMT-1	-380	2.32	6.34
CMT-2	-462	2.10	7.19

3.7 Assessment of productivity and energy consumption

Important factors of process viability are productivity and energy consumption. The latter becomes of high importance due to emerging European Commission regulations. The laser remelting process provided almost twice the productivity (4.27 h per m²) compared to the CMT process (7.41 h per m²), see Fig. 25a, even though the number of tracks were almost doubled. However, the energy consumption for the laser remelting is higher than for the CMT (see Fig. 25b) due to lower wall-plug efficiency of solid-state lasers which is ~50% [42]. In this case, only the power for the heat source is considered for both processes excluding energy use by periphery devices (robots, cooling systems etc.) for the sake of simplicity. However, scrap metal is supposed to be significantly cheaper than the production of a new filler wire and lower shielding gas consumption due to higher productivity which requires electrical energy to be produced. Therefore, the operational costs for the laser beam may be close to the CMT in term of energy consumption. If diode laser systems are considered, the electrical efficiency may be even higher than CMT since wall-plug efficiency of diode laser system is ~70%, and this is a viable option since the laser beam needs to be defocused.

The heat input in deposition of one squared meter, is similar for both processes (see Fig. 25c) and is an important factor for residual stresses and distortions. No distortions were observed after the laser remelting due to low heat input per track, 0.12 kJ/mm. In CMT cladding with 0.24 kJ/mm heat input per track, the base plate was slightly deflected after deposition of a few cladding layers. In such case, an

important factor is the frequency of the cooling phases along heat inputs. Based on these observations, the laser remelting provided much higher productivity with lower residual stresses and distortions at a slight increase of costs for energy consumption. This shows a viable alternative for the laser remelting cladding. By employing some modifications, the laser remelting can be adjusted for processing of more complex shapes, not only flat surfaces. As presented by Tuominen et al. [14], it can be used for cladding of tubes and pipes.

4 Conclusions

Based on the experimental results, the following conclusions can be made:

- Remelting with a laser beam of preplaced 2.0 mm thick stainless steel plates on a carbon steel substrate showed promising results in term of resource utilization and productivity compared to conventional arc-based cladding.
- One of the main challenges in the multi-track laser beam remelting was the non-melted areas between the plate and substrate. These areas can be minimized by optimization and adjustment of the laser beam offset and other process parameters; thus, strong metallurgical bonding can be provided.
- Low dilution of <20% was achieved for both processes which provided an acceptable corrosion resistance. Dilution can be further lowered by the optimization of process parameters.
- The use of a non-Gaussian laser beam power distribution or laser beam oscillations may further reduce dilution in

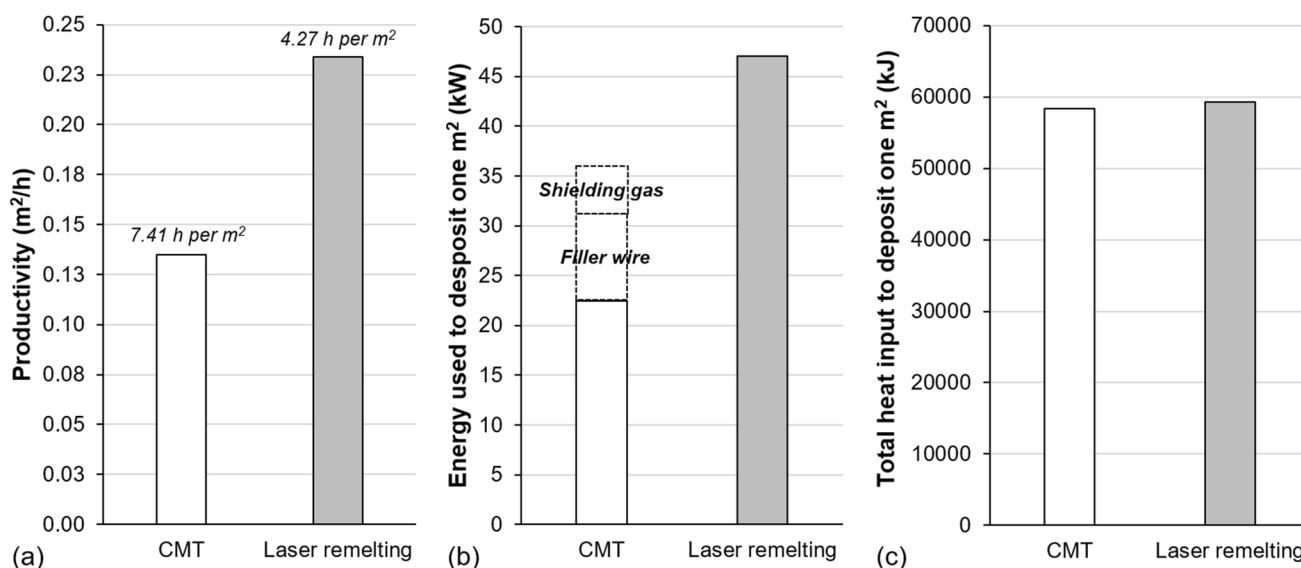


Fig. 25 Efficiency calculations of cladding methods for **a** productivity, **b** energy consumption, and **c** total heat input

remelted tracks due to more uniform weld shape since the Gaussian beam has too high beam intensity at the centre with excessive penetration depths.

- There are challenges in prediction of solidification mode due to rapid solidification speeds in both processes, especially for the laser beam remelting case which may exceed 3000 °C/s cooling rates. Therefore, only few diagrams showed consistency with the observed microstructural features. Even though the Schaeffler diagram do not consider the solidification speed, it showed a good agreement with the experimental observations compared to other methods.
- Numerical thermal modelling showed a good agreement with empirically estimated values. Therefore, PDAS and SDAS can be estimated based on the cooling rate and vice versa. Some discrepancies in data signify a necessity for improvement of the empirical data in near future for the selected materials.
- The laser-remelted tracks showed higher hardness at the intermediate layer due to a much higher cooling rate, based on both microhardness and nanoindentation, which may provide higher strength and wear resistance compared to CMT clads. However, no decarburized layer was observed for both processes providing improved strength of the heat-affected zone.
- Both processes provided almost twofold lower corrosion resistance than initial 316L stainless steel base plate due to high dilution and possible some evaporation of Cr and Ni elements. However, the laser-remelted tracks showed an improved corrosion resistance compared to the CMT cladding although it had higher delta ferrite fraction.

Supplementary Information The online version contains supplementary material available at <https://doi.org/10.1007/s00170-023-11567-y>.

Author contribution I. Bunaziv: formal analysis, data curation, software, visualization, conceptualization, methodology, validation, investigation, writing—original draft, writing—review and editing. X. Ren: project administration, conceptualization, funding acquisition, validation, writing—review and editing. A.B. Hagen: investigation, nano-indentation. EDS, writing—original draft, writing—review and editing. E.W. Hovig: numerical simulation, writing—review and editing. I. Jevremovic: corrosion testing, writing—original draft. S. Gulbrandsen-Dahl: project administration, funding acquisition, writing—review and editing.

Funding Open access funding provided by SINTEF. The work was funded by the Research Council of Norway through SFI Manufacturing under contract No. 237900. In addition, this research work is conducted on MANULAB (Norwegian Manufacturing Research Laboratory) infrastructure, co-funded by the Norwegian Research Council (Grant No: 269898).

Declarations

Competing interests The authors declare no competing interests.

Open Access This article is licensed under a Creative Commons Attribution 4.0 International License, which permits use, sharing, adaptation, distribution and reproduction in any medium or format, as long as you give appropriate credit to the original author(s) and the source, provide a link to the Creative Commons licence, and indicate if changes were made. The images or other third party material in this article are included in the article's Creative Commons licence, unless indicated otherwise in a credit line to the material. If material is not included in the article's Creative Commons licence and your intended use is not permitted by statutory regulation or exceeds the permitted use, you will need to obtain permission directly from the copyright holder. To view a copy of this licence, visit <http://creativecommons.org/licenses/by/4.0/>.

References

1. DebRoy T, Wei HL, Zuback JS, Mukherjee T, Elmer JW, Milewski JO, Beese AM, Wilson-Heid A, De A, Zhang W (2018) Additive manufacturing of metallic components – process, structure and properties. *Prog Mater Sci* 92:112–224. <https://doi.org/10.1016/j.pmatsci.2017.10.001>
2. Tušek J, Suban M (2003) High-productivity multiple-wire submerged-arc welding and cladding with metal-powder addition. *J Mater Process Technol* 133(1):207–213. [https://doi.org/10.1016/S0924-0136\(02\)00235-2](https://doi.org/10.1016/S0924-0136(02)00235-2)
3. Modenesi PJ, Reis RI (2007) A model for melting rate phenomena in GMA welding. *J Mater Process Technol* 189(1):199–205. <https://doi.org/10.1016/j.jmatprotec.2007.01.022>
4. Zhu L, Xue P, Lan Q, Meng G, Ren Y, Yang Z, Xu P, Liu Z (2021) Recent research and development status of laser cladding: a review. *Opt Laser Technol* 138:106915. <https://doi.org/10.1016/j.optlastec.2021.106915>
5. Pajukoski H, Näkki J, Thieme S, Tuominen J, Nowotny S, Vuoristo P (2016) High performance corrosion resistant coatings by novel coaxial cold- and hot-wire laser cladding methods. *J Laser Appl* 28(1):012011. <https://doi.org/10.2351/1.4936988>
6. Brueckner F, Riede M, Marquardt F, Willner R, Seidel A, Thieme S, Leyens C, Beyer E (2017) Process characteristics in high-precision laser metal deposition using wire and powder. *J Laser Appl* 29(2):022301. <https://doi.org/10.2351/1.4983237>
7. Tuominen J, Näkki J, Pajukoski H, Peltola T, Vuoristo P (2012) Recent developments in high power laser cladding techniques. *ICALEO 2012*:192–196. <https://doi.org/10.2351/1.5062441>
8. Zhang S, Xiao H, Xie H, Gu L (2014) The preparation and property research of the stainless steel/iron scrap clad plate. *J Mater Process Technol* 214(6):1205–1210. <https://doi.org/10.1016/j.jmatprotec.2014.01.006>
9. Jackson MA, Morrow JD, Thoma DJ, Pfefferkorn FE (2020) A comparison of 316 L stainless steel parts manufactured by directed energy deposition using gas-atomized and mechanically-generated feedstock. *CIRP Ann* 69(1):165–168. <https://doi.org/10.1016/j.cirp.2020.04.042>
10. Fullenwider B, Kiani P, Schoenung JM, Ma K (2019) Two-stage ball milling of recycled machining chips to create an alternative feedstock powder for metal additive manufacturing. *Powder Technol* 342:562–571. <https://doi.org/10.1016/j.powtec.2018.10.023>
11. Jackson MA, Kim A, Manders JA, Thoma DJ, Pfefferkorn FE (2020) Production of mechanically-generated 316L stainless steel feedstock and its performance in directed energy deposition processing as compared to gas-atomized powder. *CIRP J Manuf Sci Technol* 31:233–243. <https://doi.org/10.1016/j.cirpj.2020.05.014>
12. Samarjy RSM, Kaplan AFH (2017) Using laser cutting as a source of molten droplets for additive manufacturing: a new recycling

- technique. *Mater Des* 125:76–84. <https://doi.org/10.1016/j.matdes.2017.03.080>
13. Sundqvist J, Samarjy RSM (2019) High-speed imaging of droplet behaviour during the CYCLAM drop-deposition technique. *Procedia Manuf* 36:208–215. <https://doi.org/10.1016/j.promfg.2019.08.027>
 14. Tuominen J, Kaubisch M, Thieme S, Näkki J, Nowotny S, Vuoristo P (2019) Laser strip cladding for large area metal deposition. *Addit Manuf* 27:208–216. <https://doi.org/10.1016/j.addma.2019.01.008>
 15. Jemblie L, Bjaaland H, Nyhus B, Olden V, Akselsen OM (2017) Fracture toughness and hydrogen embrittlement susceptibility on the interface of clad steel pipes with and without a Ni-interlayer. *Mater Sci Eng A* 685:87–94. <https://doi.org/10.1016/j.msea.2016.12.116>
 16. Yu C, Deng Z, Liang S, Xiao H, Zhao Y (2021) Effect of pure iron interlayer on microstructure and properties of hot-rolled stainless steel clad plate. *Mater Today Commun* 28:102497. <https://doi.org/10.1016/j.mtcomm.2021.102497>
 17. Lippold JC (2015) *Welding Metallurgy and Weldability*. Wiley
 18. Oliver WC, Pharr GM (2004) Measurement of hardness and elastic modulus by instrumented indentation: advances in understanding and refinements to methodology. *J Mater Res* 19(1):3. <https://doi.org/10.1557/jmr.2004.19.1.3>
 19. Grupp M, Klinker K, Cattaneo S (2011) Welding of high thicknesses using a fibre optic laser up to 30 kW. *Weld Int* 27(2):109–112. <https://doi.org/10.1080/09507116.2011.600043>
 20. Wei PS (2010) Thermal science of weld bead defects: a review. *J Heat Transfer* 133(3):031005:031001–031022. <https://doi.org/10.1115/1.4002445>
 21. Otto A, Patschger A, Seiler M (2016) Numerical and experimental investigations of humping phenomena in laser micro welding. *Phys Procedia* 83:1415–1423. <https://doi.org/10.1016/j.phpro.2016.09.004>
 22. Allen TR, Simonds BJ, Tanner JR, Fraser JM (2020) Simultaneous in operando monitoring of keyhole depth and absorbance in laser processing of AISI 316 stainless steel at 200 kHz. *Procedia CIRP* 94:419–424. <https://doi.org/10.1016/j.procir.2020.09.157>
 23. Jiang Z, Chen X, Li H, Lei Z, Chen Y, Wu S, Wang Y (2020) Grain refinement and laser energy distribution during laser oscillating welding of Invar alloy. *Mater Des* 186:108195. <https://doi.org/10.1016/j.matdes.2019.108195>
 24. Porter DA, Easterling KE (2021) *Phase transformations in metals and alloys*. 4th ed. CRC Press. <https://doi.org/10.1201/9781003011804>
 25. Lin Z, Wang S, He J, Liu B, Chen C, Feng J, Zhang X, Fang W, Yin F (2020) The effect of Ni Interlayer on the hot-rolled and quenched stainless steel clad plate. *Materials* 13(23):5455. <https://doi.org/10.3390/ma13235455>
 26. Olson DL (1985) Prediction of austenitic weld metal microstructure and properties. *Weld J* 64(10):281–295
 27. Kotecki DJ, Siewert TA (1992) WRC-1992 Constitution Diagram for Stainless Steel Weld Metals: A Modification of the WRC-1988 Diagram. *Weld J* 71:171–178
 28. Wang L, Xue J, Wang Q (2019) Correlation between arc mode, microstructure, and mechanical properties during wire arc additive manufacturing of 316L stainless steel. *Mater Sci Eng A* 751:183–190. <https://doi.org/10.1016/j.msea.2019.02.078>
 29. Lippold JC (1994) Solidification behavior and cracking susceptibility of pulsed-laser welds in austenitic stainless steels. *Weld J* 73:6. <https://www.osti.gov/biblio/7167543>
 30. Elmer JW, Allen SM, Eagar TW (1989) Microstructural development during solidification of stainless steel alloys. *Metall Mater Trans A* 20(10):2117–2131. <https://doi.org/10.1007/BF02650298>
 31. Suutala N (1983) Effect of solidification conditions on the solidification mode in austenitic stainless steels. *Metall Mater Trans A* 14(1):191–197. <https://doi.org/10.1007/BF02651615>
 32. Kamiya O, Kumagai K, Kikuchi Y (1992) Effects of delta ferrite morphology on low-temperature fracture toughness of austenitic stainless steel weld metal. *Weld Int* 6(8):606–611. <https://doi.org/10.1080/09507119209548250>
 33. Wang Q, Chen S, Lv X, Jiang H, Rong L (2022) Role of δ -ferrite in fatigue crack growth of AISI 316 austenitic stainless steel. *J Mater Sci Technol* 114:7–15. <https://doi.org/10.1016/j.jmst.2021.10.008>
 34. Gilath I, Signamarcheix JM, Bensussan P (1994) A comparison of methods for estimating the weld-metal cooling rate in laser welds. *J Mater Sci* 29:3358–3362. <https://doi.org/10.1007/BF00356685>
 35. Huang Y, Ansari M, Asgari H, Farshidianfar MH, Sarker D, Khamesee MB, Toyserkani E (2019) Rapid prediction of real-time thermal characteristics, solidification parameters and microstructure in laser directed energy deposition (powder-fed additive manufacturing). *J Mater Process Technol* 274:116286. <https://doi.org/10.1016/j.jmatprotec.2019.116286>
 36. Katayama S (1984) Matsunawa A (1984) Solidification microstructure of laser welded stainless steels. *ICALEO* 2:60–67. <https://doi.org/10.2351/1.5057623>
 37. Alali M, Todd I, Wynne BP (2017) Through-thickness microstructure and mechanical properties of electron beam welded 20mm thick AISI 316L austenitic stainless steel. *Mater Des* 130:488–500. <https://doi.org/10.1016/j.matdes.2017.05.080>
 38. Pickin CG, Williams SW, Lunt M (2011) Characterisation of the cold metal transfer (CMT) process and its application for low dilution cladding. *J Mater Process Technol* 211(3):496–502. <https://doi.org/10.1016/j.jmatprotec.2010.11.005>
 39. Qian L, Li M, Zhou Z, Yang H, Shi X (2005) Comparison of nano-indentation hardness to microhardness. *Surf Coat Technol* 195(2):264–271. <https://doi.org/10.1016/j.surfcoat.2004.07.108>
 40. Murkute P, Pasebani S, Isgor OB (2019) Production of corrosion-resistant 316L stainless steel clads on carbon steel using powder bed fusion-selective laser melting. *J Mater Process Technol* 273:116243. <https://doi.org/10.1016/j.jmatprotec.2019.05.024>
 41. Meng Y, Kang K, Gao M, Zeng X (2018) Microstructures and properties of single-pass laser-arc hybrid welded stainless clad steel plate. *J Manuf Process* 36:293–300. <https://doi.org/10.1016/j.jmapro.2018.10.022>
 42. Gapontsev V, Moshegov N, Berezin I, Komissarov A, Trubenko P, Miftakhutdinov D, Berishev I, Chuyanov V, Raisky O, Ovtchinnikov A (2017) Highly-efficient high-power pumps for fiber lasers. In: *SPIE LASE Proceedings 2017. High-Power Diode Laser Technology XV*. <https://doi.org/10.1117/12.2250634>

Publisher's note Springer Nature remains neutral with regard to jurisdictional claims in published maps and institutional affiliations.